Geophysical Journal International

Geophys. J. Int. (2023) **235,** 1832–1848
Advance Access publication 2023 August 21
GJI Seismology

https://doi.org/10.1093/gji/ggad324

Sp converted waves reveal the structure of the lithosphere below the Alps and their northern foreland

Rainer Kind,[1,2] Stefan M. Schmid,[3] Felix Schneider,[2] Thomas Meier,[4] Xiaohui Yuan,[2] Ben Heit,[2] Christian Schiffer[5] and AlpArray and SWATH-D Working Groups[*]

[1]*Deutsches GeoForschungsZentrum GFZ, Section Seismology,* 14473 *Potsdam, Germany. E-mail: kind@gfz-potsdam.de*
[2]*Freie Universität Fachbereich Geowissenschaften, Fachrichtung Geophysik,* 12249 *Berlin, Germany*
[3]*Eidgenössische Technische Hochschule ETH, Institut für Geophysik,* 8006 *Zürich, Switzerland*
[4]*Christian-Albrechts-Universität, Institut für Geowissenschaften,* 24118 *Kiel, Germany*
[5]*Department of Earth Sciences, Uppsala University,* 75236 *Uppsala, Sweden*

Accepted 2023 August 9. Received 2023 July 19; in original form 2023 February 18

SUMMARY

The structure of the lithosphere is reflecting its evolution. The Moho of the European lithosphere has already been studied intensively. This is, however, not yet the case for the lower boundary of the lithosphere, that is the lithosphere–asthenosphere boundary (LAB). We are using S-to-P converted seismic waves to study the structures of the Moho and the LAB beneath Europe including the greater Alpine Area with data from the AlpArray project and the European networks of permanent seismic stations. We use plain waveform stacking of converted waves without deconvolution and compare the results with stacking of deconvolved traces. We also compare Moho depths determinations using S-to-P converted waves with those obtained by other seismic methods. We present more detailed information about negative velocity gradients (NVG) below the Moho. Its lower bound may be interpreted as representing the LAB. We found that the thickness of the European mantle lithosphere is increasing from about 50°N towards the Alps along the entire east–west extension of the Alps. The NVG has also an east dipping component towards the Pannonian Basin and the Bohemian Massif. The Alps and their northern foreland north of about 50°N are surrounded in the east, west and north by a north dipping mantle lithosphere. Along 50°N, where the NVG is reversing its dip direction towards the north, is also the area along which the volcanoes of the European Cenozoic Rift System are located. Our results possibly indicate that the Alpine collision has deformed the entire lithosphere of the Alpine foreland as far north as about 50°N.

Key words: Body waves; Waveform inversion; Crustal structure.

INTRODUCTION

Seismic methods continue to play a significant role in imaging tectonic structures. Especially steep angle seismic studies essentially increased our knowledge about the crustal structure of the European lithosphere (e.g. Meissner *et al.* 1991). Most deep seated tectonic structures within the mantle have been studied by controlled source long range seismic experiments (e.g. Kind 1974). Receiver function studies have shown that stacking methods may raise small seismic phases, like converted waves, above the noise level and lead to new results. Thereby they play a significant role in upper mantle studies, similar to the steep angle seismic in crustal studies. Many studies addressing the lithosphere–asthenosphere boundary (LAB) and the mid-lithospheric discontinuity (MLD) in the upper mantle, have been carried out using *P*- and *S*-receiver functions (examples are Abt *et al.* 2010 on a continental scale or Schiffer *et al.* 2015 in east Greenland). *P*- and *S*-receiver functions are also used to study the influence of plume conduits on the upper mantle seismic discontinuities (e.g. Li *et al.* 2000). Kosarev *et al.* (1999) and Kind *et al.* (2002) have studied the continent–continent collision in Tibet using receiver functions. They imaged the subducting Indian and Asian mantle lithosphere below the southern and northern parts of the Tibetan Plateau down to 200 km. In the Alpine continent–continent collision zone Handy *et al.* (2021) imaged with *P*-wave tomography the south-dipping European slab and a detached slab below the eastern Alps. They observed a 180-km-thick European lithosphere, which differs greatly from the 100 to 120 km thickness of the with seismic body waves determined European lithosphere, suggested, for example by Geissler *et al.* (2010). Our goal is to study the structure of the European Plate in the greater Alpine collision zone with

[*]A list of the Working Groups members can be found in the Acknowledgements.

S-receiver functions using the recently available large amount of new data.

In most cases the receiver function technique uses deconvolution before stacking in order to equalize the waveforms of different earthquakes. This step may lead to failures in the deconvolution process as shown by Kind *et al.* (2012), Kind *et al.* (2020) and Krueger *et al.*(2021). Hua *et al.* (2023) studied upper mantle discontinuities on a global scale using *S*-receiver functions. They especially discuss possible problems due to the application of deconvolution. Their conclusion is that deconvolution causes no problems. However, we will show below that deconvolution may cause significant problems if the noise level is high.

Besides improving the images of the NVGs located within the European mantle, the second goal of our study is the comparison of Moho depth determinations in central Europe obtained by Sp conversions with those inferred by other seismic methods.

DATA AND METHOD

Earlier work on the AlpArray project (Kind *et al.* 2021) was extended by adding data from permanent seismic broad-band networks in larger regions of Europe beyond the AlpArray (Hetényi *et al.* 2018) to study the Moho and the mantle lithosphere at a larger scale based on observations of S-to-P converted teleseismic signals. A map of the stations used is shown in Fig. 1. Most data were obtained from the AlpArray project. All networks providing data to our work are listed in the Acknowledgements. Most of them provide open data. The data set comprises about 2700 permanent and temporary stations used. All data have been copied from the EIDA archives in several countries. For most portals this worked without any problem. We selected events with magnitudes greater than 5.4 and copied continuous data in a time window of 300 s before and after the theoretical onset of the *S* wave.

The basic idea of our method is to study weak S-to-P converted waves by stacking of original seismic broad-band records. The influence of the different source regions on the recorded waveforms would be reduced by the summation and the effects of the identical near station region would be amplified. Summation is necessary to suppress the noise since in most cases the amplitudes of the converted signals are below the noise level in individual records. They are only a few per cent of the incident SV wave. Some processing steps are necessary before summation. We used the Seismic Handler software package for data processing (Stammler 1993; https://www.seismic-handler.org). The following processing steps have been applied:

(i) Rotation of the Z, N, E components into the P, SV, SH coordinate system: Theoretical backazimuths and incidence angles are used. The incidence angles are computed using the IASP91 global Earth model (Kennett & Engdahl 1991).

(ii) Providing a common time scale for all records by using the SV arrival times as zero time: The arrival of the SV signals on the individual SV components were picked by the algorithm of Baer & Kradolfer (1987). The signal-to-noise threshold was chosen at 4 and the amplitude was not allowed to fall below that limit for a duration of at least 1 s. Negative signs of the SV signals were reversed. All traces have been normalized by the maximum amplitude of the SV signal within the first 3 s after the onset. As a second noise criterion it was chosen that the noise before the expected Moho conversion on the P component should not be bigger than 50 per cent of the SV signal. We obtained more than 80 thousand records by applying these criteria. The picked SV onset times of the individual records have not been checked visually. However, the stacks of subgroups have been checked visually. We mention that the automatically picked arrival times of the SV signal are on average over all traces about 1.2 s later than what we would pick visually. Therefore, we shifted all traces manually by this amount.

(iii) For time domain stacking a distance (or slowness) moveout correction was applied for a hypothetical slowness of 6.4 s/° using the IASP91 global reference model (Kennett & Engdahl 1991). This slowness value was chosen because it is frequently used in P receiver function processing and it makes Sp precursor times directly comparable with the according Ps delay times.

(iv) A 30 s high pass filter was also applied to suppress longer period noise.

(v) Common conversion point stacking: Coordinates of Sp piercing points for all traces are computed for a chosen depth using the IASP91 model and traces with piercing points within a certain geographical area were stacked, independent of the location of the recording station.

Precursor times of Moho conversions have been obtained the following way:

We computed theoretical piercing points for a conversion depth of 50 km and summed all traces within piercing point cells of 1° latitude and longitude. We covered the entire region of central Europe between the Alps and Scandinavia with such cells. The number of traces within each cell is given in Table 1 of the Supporting Information. It ranges from just a few traces or several tens of traces in Scandinavia to about thousand traces in some of the Alpine regions. This implies that we obtain an average value of the Moho depth for each 1° × 1° cell. The stability of the averaged Moho signal depends on the azimuthal coverage of the source regions, which is not perfect.

We are aware that many published Moho depth determinations have higher lateral resolution compared to our data set. However, our goal is not to improve the resolution of the Moho map. Higher resolution can be obtained with other methods, for example with shorter period *P*-receiver functions. Instead, the goal of our *S*-receiver function study of the Moho is the comparison of different methods, and additionally, the check of large-scale agreement of results obtained with different methods. In the Alps we could have used smaller cells due to higher data density. However, we have chosen to use the same cell size for the entire study area for easier comparison.

We visually selected only cells with clearly identifiable Moho signals in the stacks. We have chosen not to pick arrival times of the Moho signals with an automatic method like we used for picking the SV arrival times. Instead, we compared the waveforms of the SV signal with the waveforms of the Moho signals. This was done by visually shifting the SV signals of stacked traces in time until it reached the best fit with the Moho signal. The applied time shift represents the Moho precursor time, which is used to compute the depth of the Moho with an assumed velocity model (IASP91). The whole procedure is explained in Fig. 2(a) for a number of cells. The coordinates of the centre of the cells used are given on the left of Fig. 2(a). The black traces are the stacked SV components for each cell with amplitudes reduced to 20 per cent. The red traces are the *P* components with the Moho conversions as biggest signals. The grey traces are the shifted SV traces. In most cases it appears that the Moho signals fit the SV signals reasonably well.

Fig. 2(b) shows the *P* traces from Fig. 2(a) (red traces) in an east–west profile around 47°N latitude along the strike of the Alpine orogen with the resulting Moho precursor times marked by green

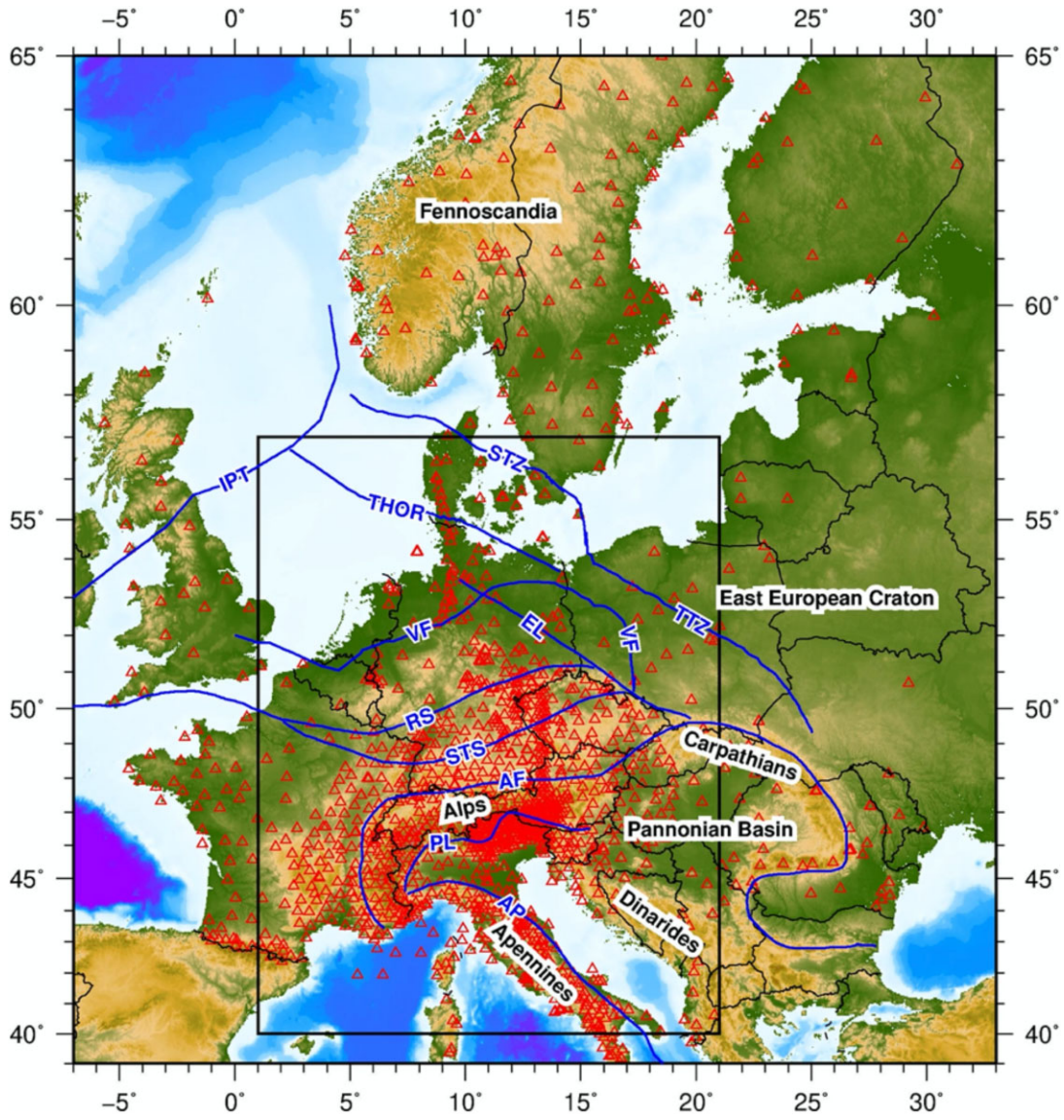

Figure 1. Map showing the locations permanent and temporary seismic stations. The stations within the square are used in this study. Most stations in the Alpine area are temporary stations within the AlpArray Project, the dense cloud of stations in the eastern Alps are mostly from the SWATH-D Project. AF, Alpine Front; AP, Apennine Front. EL, Elbe Line; IPT, Iapetus Suture; PL, Periadriatic Line; RS, Rheic Suture; STS, Saxothuringian-Moldanubian Suture; STZ, Sorgenfrei-Tornquist Zone; THOR, Thor Suture; TTZ, Tornquist-Teysseire Zone and VF, Variscan Front.

dots. Moho signals are coloured in blue (velocity increase downward) and velocity decrease downward are coloured in red. Many more similar profiles are shown in the Supporting Information. The Supporting Information also provides in Table 1(a) list of the coordinates of the centres of all cells used along with the Moho precursor times for a slowness (related to the incidence angle or epicentral distance) of 6.4 s deg^{-1}. The Moho depth is calculated for the IASP91 model. The number of traces summed in each cell is also listed in Table 1 in the Supporting Information. This number is also important for the quality of the Moho signals. In a few exceptional cases we think that a few traces might already be sufficient. However, in most cases at least several tens of traces are necessary. In a number of cases, it was difficult to fit the SV and Sp waveforms because of a complicated structure of the signals. An example is shown in the east–west profile in Fig. 3(a), located around 54°N latitude, that is approximately along the German coast of the North Sea and Baltic Sea. As usual we matched the waveform of the biggest precursor Sp signal with the SV signal. However, in the longitude range between 7°E and 11°E the large Moho signal marked by the green dots has a weak positive precursor near about 7 s (marked MOHO-S). This could be explained by a second downward velocity increase below the Moho near 65 km depth (right scale of Fig. 3a), which might be interpreted as a remnant of a fossil subduction or a petrological discontinuity.

Fig. 3(b) shows examples of summed SV signals along the same east–west profile as shown in Fig. 3(a). Fig. 3(b) serves for demonstrating the influence of the near station structure on the waveforms of the incident seismic waves. The scale of the normalized amplitudes is given on the left side of this figure. The normalization of SV to 1 was done for each individual trace. After stacking the normalized amplitude is no more equal to 1 because the maxima of SV do not occur at exactly the same time in the individual traces. The SV signals are lined up along the picked SV arrival times. We note a significant difference in the waveforms of SV along the profile.

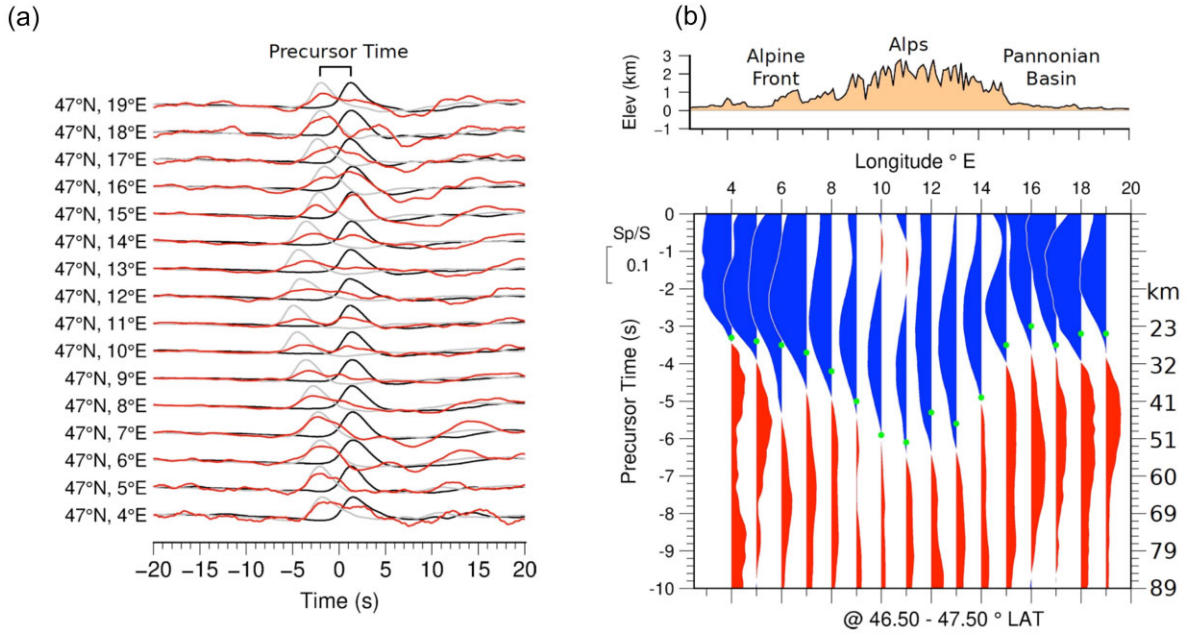

Figure 2. (a) Red traces: stacked S-to-P converted signals from the Moho with piercing points at 50 km depth. Black traces: Stacked and amplitude normalized SV signals. Grey traces: Shifted SV signals to fit the Moho waveform for determination of the precursor times of the Moho conversion. Zero time is the SV arrival time before stacking. Coordinates on the left side are the centres of the 1° × 1° latitude and longitude cells used for stacking. (b) Example of an east–west profile between 46.5° and 47.5° latitude with Moho conversions (blue) and weaker conversions (red) from velocity reductions below the Moho. Green dots are Moho precursor times determined by waveform comparison and not by picking of onsets.

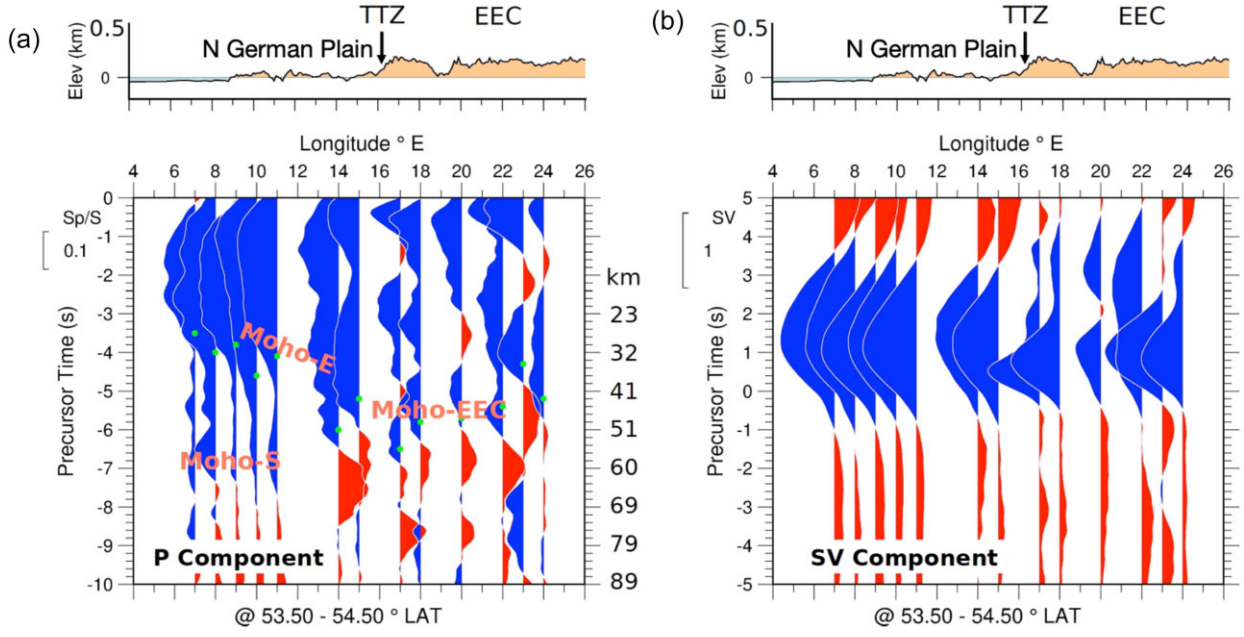

Figure 3. East–west profile located between 53.5° and 54.5° latitude. (a) *P*-wave component with Moho conversions and approximate onsets marked by green dots. (b) SV component of the same stacked records shown in (a). Its signal form strongly changes across the Tornquist-Teysseire Zone, which shows that the SV signal form depends on the local geological structure beneath the station. European Moho: Moho-E; Moho of the east European craton: Moho-EEC; Scandinavian Moho: Moho-S.

Between 7 and 15°E longitude the duration of SV is about 3 s, and between 17 and 24°E longitude it is about 1–2 s. This change occurs across the Tornquist-Teisseyre Zone, which separates the East European Platform from the Mesozoic Europe. We conclude that the differences in the SV signals are probably caused by differences in the crustal properties, especially of the uppermost part of the crust in both regions.

Although we have used in our Moho depth determinations common conversion point cells with a size of 1° longitude and 1° latitude, we show in the following Fig. 4 that much higher resolutions are also

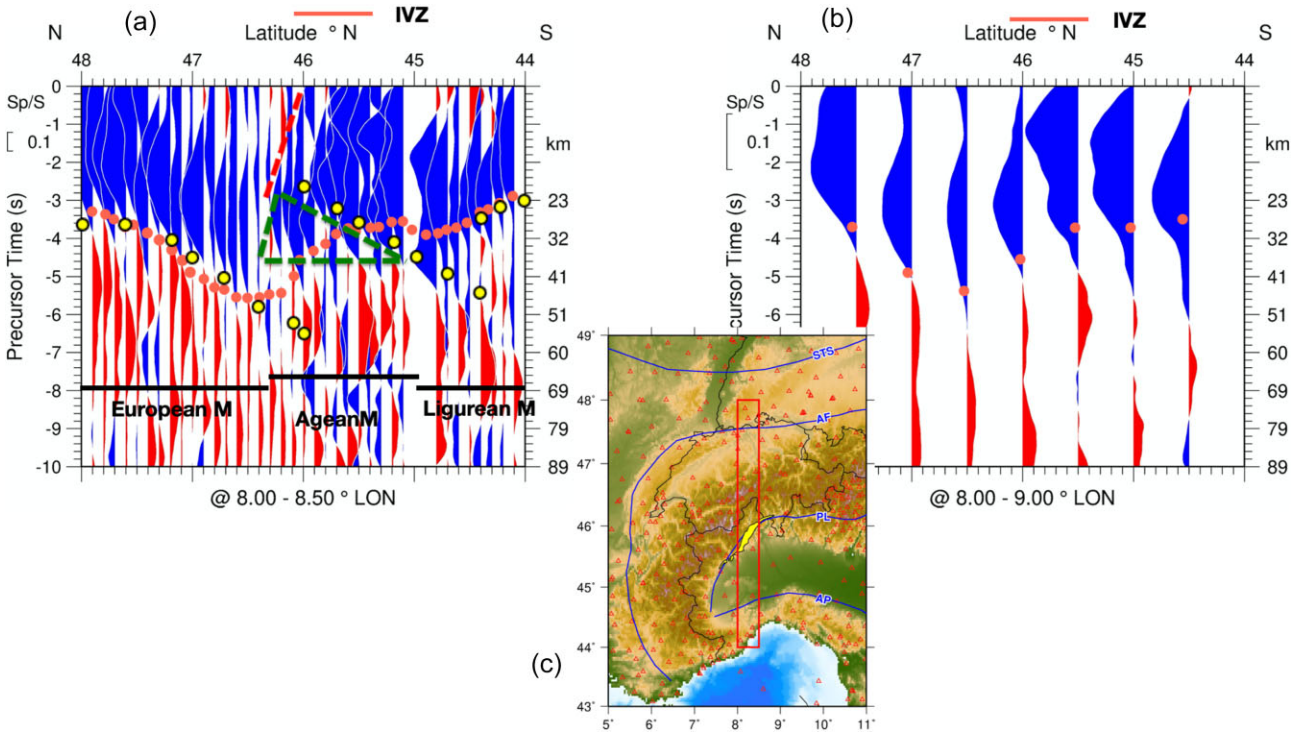

Figure 4. N–S profile between 8.0 and 8.5°E across Alps, Ivrea Zone and Po-Plain. Note that the Moho is segmented into European, Adriatic and Ligurian Moho according to Spada *et al.* (2013). (a) Piercing point cells are 0.5° in east–west direction but 0.1° in north–south direction. (b) Similar to (a) but piercing point cells are 0.5° in north–south direction. Red dots in (a) and (b) are Moho depths from Grad *et al.* (2009), black bordered yellow dots in (a) are Moho depths from Spada *et al.* (2013). Ivrea Zone (IVZ) in (a) and (b) is marked by a red line and in (c) as yellow area. Red dashed line and green triangle in (a) mark the Periadriatic Line and the Mantle Wedge (Schmid *et al.* 2017).

possible with *S*-receiver functions if the ray density is high enough. Fig. 4(a) shows a north–south profile with piercing point cells 0.1° wide in north–south direction and 0.5° wide in east–west direction. As a result the Moho signals are clearly imaged in this figure. The red dots are Moho depths obtained by Grad *et al.* (2009). They fit our Moho observations (first arrivals of blue phases) north of 46°N well. There are exceptions south of the Alps (south of 46°N). The black bordered yellow dots are Moho depths from Spada *et al.* (2013). The Spada data show significant jumps at 46°N and 44.4°N. This jump at 44.4°N is not observed in the blue Sp signals. The profile in Fig. 4(a) is cutting through the Ivrea Zone (Schmid *et al.* 2017) which is marked in Fig. 4(c). The mantle wedge (dashed green triangle) and the Periadriatic Line (dashed red line) are also marked in Fig. 4(a) (Schmid *et al.* 2017). The Adriatic crust south of the Periadriatic Line contains many sources for S-to-P converted waves. Their structure, however, still cannot be resolved with longer period *S* waves, which we are using. In Fig. 4(b) the same profile as in (a) is shown for comparison however with a latitude spacing of 0.5°. The difference in resolution is obvious and demonstrates the advantage of a high ray density, which permits smaller sizes of common conversion point cells.

The question if deconvolution in receiver function processing could potentially cause problems was discussed controversially (see Kumar *et al.* 2010; Kind *et al.* 2020; Krueger *et al.* 2021; Hua *et al.* 2023). The debate focused on the influence of sidelobes. In Fig. 5, we provide new evidence which increases doubts regarding the usage of deconvolution for studies of weak converted phases. We are comparing plain stacking of signals with pre- and post-stacking of deconvolved traces. Post-stacking deconvolution means first stacking of traces and deconvolution after that. Pre-stacking deconvolution means deconvolution of each trace first and stacking after that. Plain stacking does not use deconvolution. In the case of post-stacking deconvolution, weak phases, also below the noise level, may be enhanced by stacking and the subsequent deconvolution will just modify the shape of the phases. In the case of pre-stacking deconvolution, deconvolution of the individual traces with signals below the noise level might just change the noise and destroy the weak converted signals. In case of plain stacking, onsets of the SV and the Moho conversions may be picked directly from the summation trace (Fig. 5a). If deconvolution is used times are picked at the maxima of the SV and Moho wave forms (Fig. 5b). In Figs 5(c)–(e) plain stacks, pre- and post-stack deconvolved profiles are shown, respectively. Moho and NVG signals are marked. A very similar Moho and north dipping NVG signals can be seen in the plain stacking and the post-stacking deconvolution (Figs 5c and e). The converted NVG signals of the pre-stacking deconvolution (Fig. 5d) have no similarity with the results from plain stacking and post-stack deconvolution. The larger Moho signals are less damaged by the pre-stack deconvolution. We used plain stacking only in order to avoid possible problems of deconvolution.

OBSERVATIONS

Moho depth

Plots of the stacked traces in 1° × 1° cells with useful data are shown in the Supporting Information in Slides 5–29 for east–west profiles and in Slides 31–48 for north–south profiles along with a table listing the obtained Moho precursor times and Moho depths (Table 1 in the Supplementary Information). These Moho depths

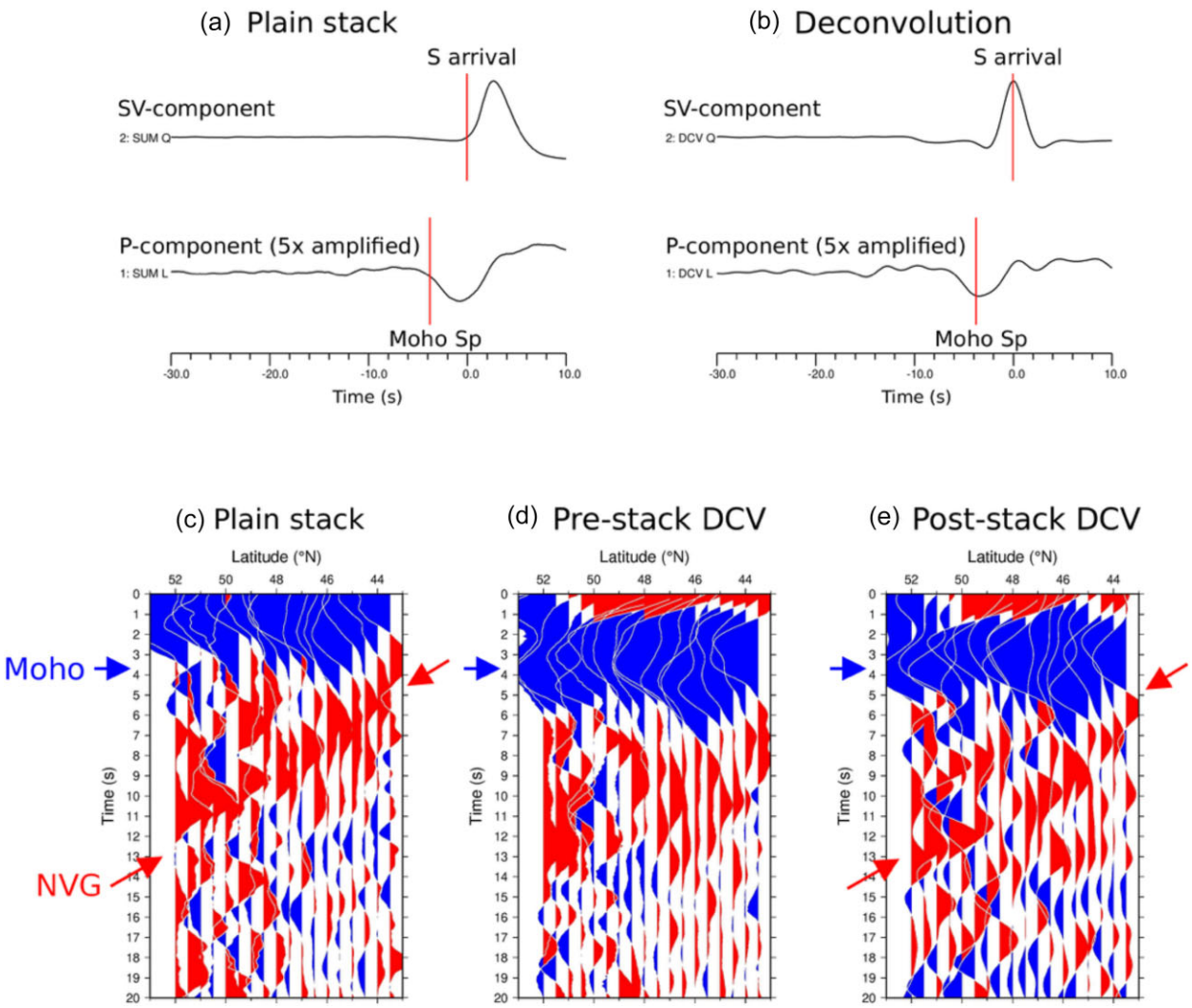

Figure 5. Comparison of stacking of plain traces and stacking of deconvolved traces. (a) Plain stacking of individual traces along a N–S profile centred on longitude of 6°E (similar to Fig. 8a). In total there are 2586 SV wave records selected with piercing points at 100 km depth located close to the profile. For each individual trace the onset of the SV wave is picked on the SV component and *P* components are aligned along these onsets. (b) Deconvolved stacks. The maximum of the deconvolved SV component is used for alignment and times of converted waves (*P* component) are also picked at the maximum of the converted signal. (c) North–south profile with plain stacking. (d) N–S profile of pre-stacking deconvolution. (e) N–S profile of post-stacking deconvolution. The NVG results of (c) and (e) agree reasonable well. The pre-stacking deconvolution in (d) shows a very different picture of the converted waves.

are displayed in the map of Fig. 6(a) as colour-coded filled circles within the European map of the Moho depth provided by Grad *et al.* (2009) and shown in background colours. There are many regional Moho depth determinations with *P*- and *S*-receiver functions. A comprehensive review is given by Knapmeyer-Endrun *et al.* (2014). Spada *et al.* (2013) also published a detailed Moho map of the Alpine area while Ziegler & Dèzes (2006) published a European Moho map. Here we restrict the comparison of our data mainly to the map of Grad *et al.* (2009). This map was obtained on the basis of seismic profiles, surface waves analysis and receiver functions. We emphasize that we did not apply any smoothing between results of different cells. We checked locations with the largest differences between the two maps and kept only those where the waveform fit was considered sufficient. The accuracy of the depth determinations in the Grad map was estimated as ±3–6 km. The accuracy of our determinations of Moho precursor times of the averaged signals within the 1° × 1° cells is estimated as ±0.2 s if a good quality Moho signal is overlaid by the SV signal. This theoretically corresponds to about ±2 km depth using the IASP91 global velocity model and a slowness of 6.4 s deg^{-1}. However, in cases of not very clear waveforms, a wrong signal could be picked, which could lead to much larger differences. In complex areas the 1° × 1° cells will be too large for detailed and accurate Moho maps. The reader may check these estimates by comparing the SV signals and the Moho waveforms of all traces in the figures provided in the Supporting Information.

For easier comparison of our depth results with those of Grad *et al.* (2009), Fig. 6(b) also provides a map that depicts the differences in Moho depths in Fig. 6(a). White dots indicate differences of less than ±5 km. It is obvious that the entire region of the Variscan Europe is dominated by such white dots. The Alpine collision region and the region south of the coast of the Baltic Sea and Scandinavia show much larger differences in the Moho depths. In the Alpine region this is probably due to stronger heterogeneities caused by the plate collision and due to different resolutions and different smoothing in the two methods. In Scandinavia it might be due

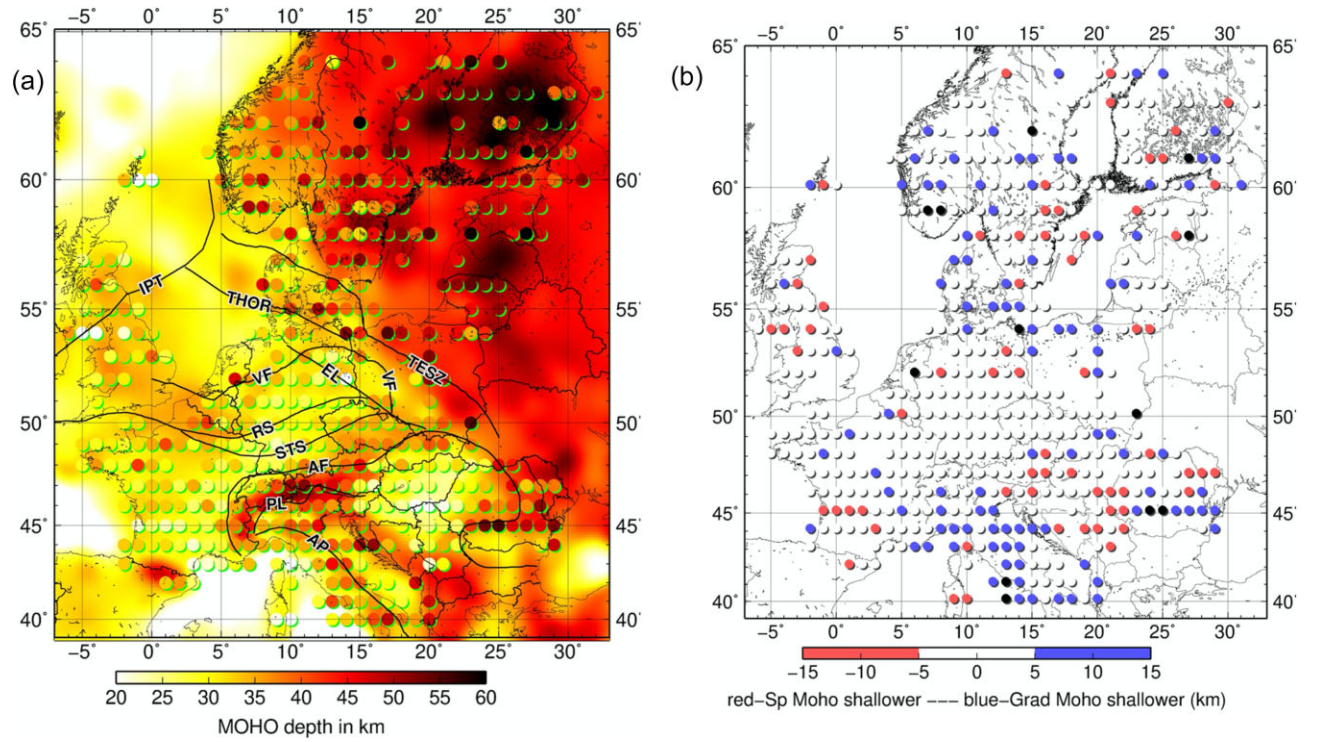

Figure 6. (a) Comparison between our determinations of Moho depths in Central Europe with those by Grad *et al.* (2009). Background colours indicate the data obtained by Grad *et al.* (2009), colours of the dots are our values. (b) Map of the differences in Moho depths between the two methods.

to a still insufficient amount of data. Slide 2b in the Supporting Information shows a diagram of the differential Moho depth as function of the Sp Moho depth. This figure shows the majority of the data points agree within ±5 km with each other. The three east–west profiles along 50°N, 47°N and 45°N in Slides 19, 22 and 24 in the Supporting Information show the Grad Moho depths marked in the Sp data. The agreement is very good in Slide 19 in the Variscan area and in Slide 22 approximately along the strike of the Alps. The scatter in Slide 24 is large in our data but also in the data of Grad et al. Therefore this likely indicates a complication of the Moho in this area. Slides 37 and 40 in the Supporting Information provide this comparison also for four north–south profiles. Within the Variscan area (between the Variscan Front in northern Germany and Alpine Front) the agreement is also very good. However, the differences are larger outside the Variscan area. Grad & Tiira (2012) also discuss differences of a European Moho map based only on receiver functions with the map of Grad *et al.* (2009). They attribute most of the differences to the different crustal models used for the depth calculation. Our confirmation of a relatively homogeneous Moho across the Variscan orogenies in central Europe supports an idea proposed by Meier *et al.* (2016) who discussed reworking of the lower crust and Moho during or after the Variscan orogenies.

Sub-Moho structures

Fig. 7 shows the location of seismic profiles indicating converted waves (NVGs) that are shown in Figs 8–13. The north–south profiles are displayed in Figs 8–11 and the east–west profiles in Figs 12 and 13, respectively. The widths of the profiles in Fig. 7 are marked by black lines. We chose narrower profile widths where the dip of the European mantle lithosphere is rapidly changing in east–west direction, that is near 6° and 14° longitude. The blue dots in Fig. 7 mark the approximate locations of the Quaternary volcanic Eifel fields, the Miocene Vogelsberg volcanic field and the Upper Cretaceous to Quaternary volcanism of the Eger Graben (from west to east).

The term ‘NVG zones’, frequently used in seismic investigations, aims at locating seismic discontinuities characterized by downward decreasing velocities in the mantle lithosphere. The question whether or not NVG zones mark the LAB in a thermal and/or rheological sense is still not satisfyingly answered, since seismic data are only one part of the characteristics defining that boundary. Thermal modelling is needed to identify the LAB. Hence, we prefer to use the term NVG as we provide only seismic evidence. Many questions regarding mantle dynamics, particularly in the eastern Alps, are still much disputed, especially regarding the slab structure. The recent seismic AlpArray and SWATH-D experiments (Heit *et al.* 2017; Hetényi *et al.* 2018) significantly expanded the amount of data and our general knowledge. In spite of this there are still many open questions, particularly concerning the eastern Alps, for example the dip direction of the slab below the eastern Alps or the thickness of the European lithosphere (e.g. Kind *et al.* 2017, 2021; El-Sharkawy *et al.* 2020; Kästle *et al.* 2020; Paffrath *et al.* 2021a,b; Bianchi *et al.* 2021; Handy *et al.* 2021; Plomerová *et al.* 2022; Rajh *et al.* 2022; Mroczek *et al.* 2023). For the stacking of traces addressing the sub-Moho structure we have computed coordinates of theoretical S-to-P conversions (piercing points) at 100 km depth for all traces. Then we defined geographic rectangle cells and stacked all traces with piercing point coordinates within such a cell (common conversion point stacking). This procedure implies that we are focus at 100 km depth, which is at about 11 s precursor time using the IASP91 model. The precursor times of the converted waves in Figs 8–13 are shown on the left of the profiles and the estimated depth on the right. The

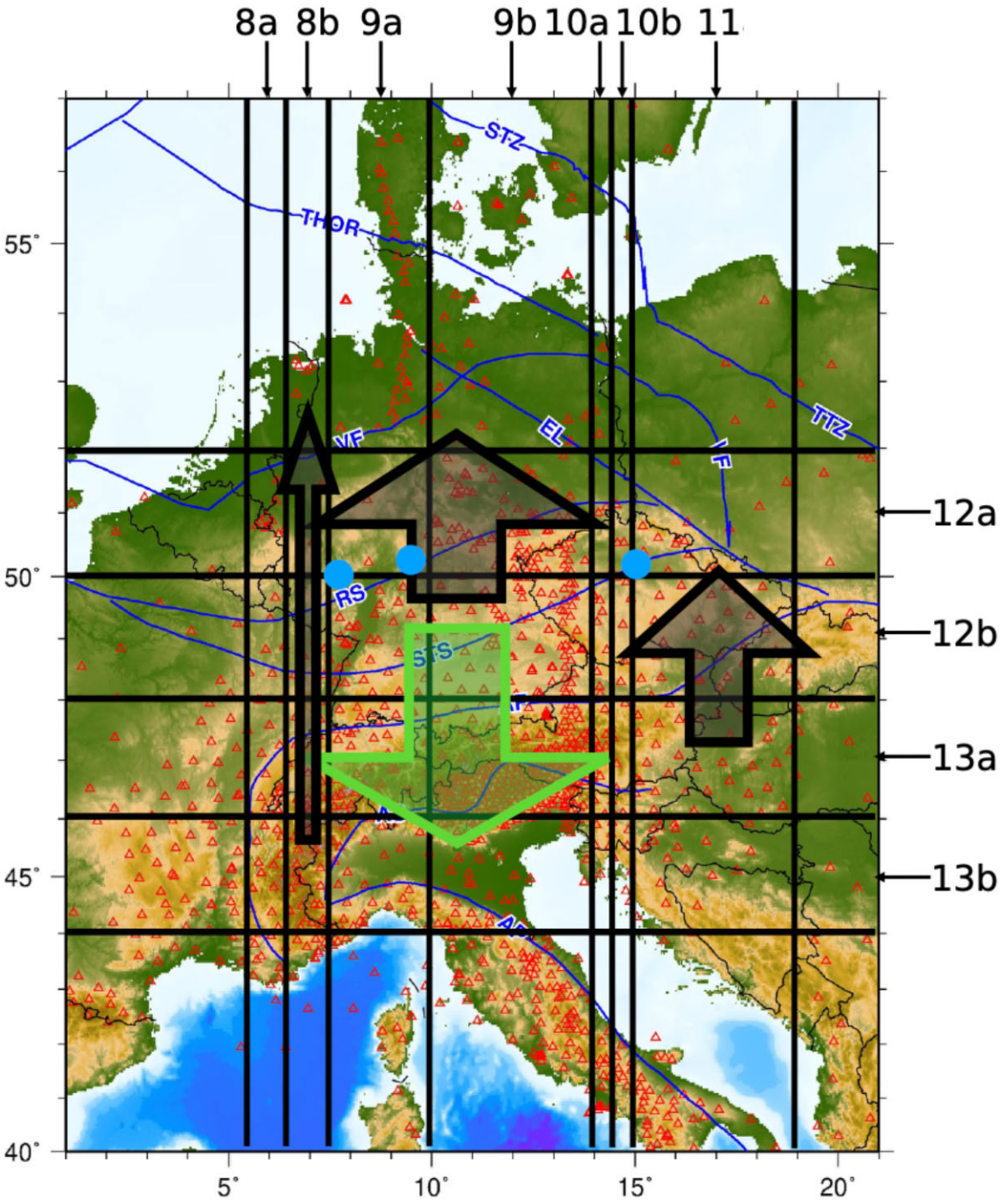

Figure 7. Location of seismic profiles shown in Figs 8–13. Note that the widths of the profiles strongly vary. Their boundaries are marked by black lines. The figure numbers of all profiles are marked. The green and black arrows mark south and north dipping Negative Velocity Gradient below the Moho, respectively. More NVG profiles are shown in the Slides 50–64 in the Supporting Information.

precursor times are observed times without any model involved, whereas the depths given on the right requires a velocity–depth model. Profiles with cell sizes of 1° × 1° in longitude and latitude are shown in the Supporting Information providing an overview of the entire area. From visual inspection of these profiles and many additional test profiles we judged the similarity and dissimilarity of neighbouring profiles for identifications of discontinuities.

Observations along north–south profiles

Figs 8–11 present north–south profiles with very different profile widths. In all these profiles we observe more or less coherent NVG phases with first arrivals approximately marked by straight lines. Fig. 8 shows two profiles obtained by choosing cell sizes of 0.5° latitude 1.0° longitude (see Fig. 7 for the locations). Note that the NVG phases marked in Fig. 8(a) (at 6°E) and Fig. 8(b) (at 7°E) are

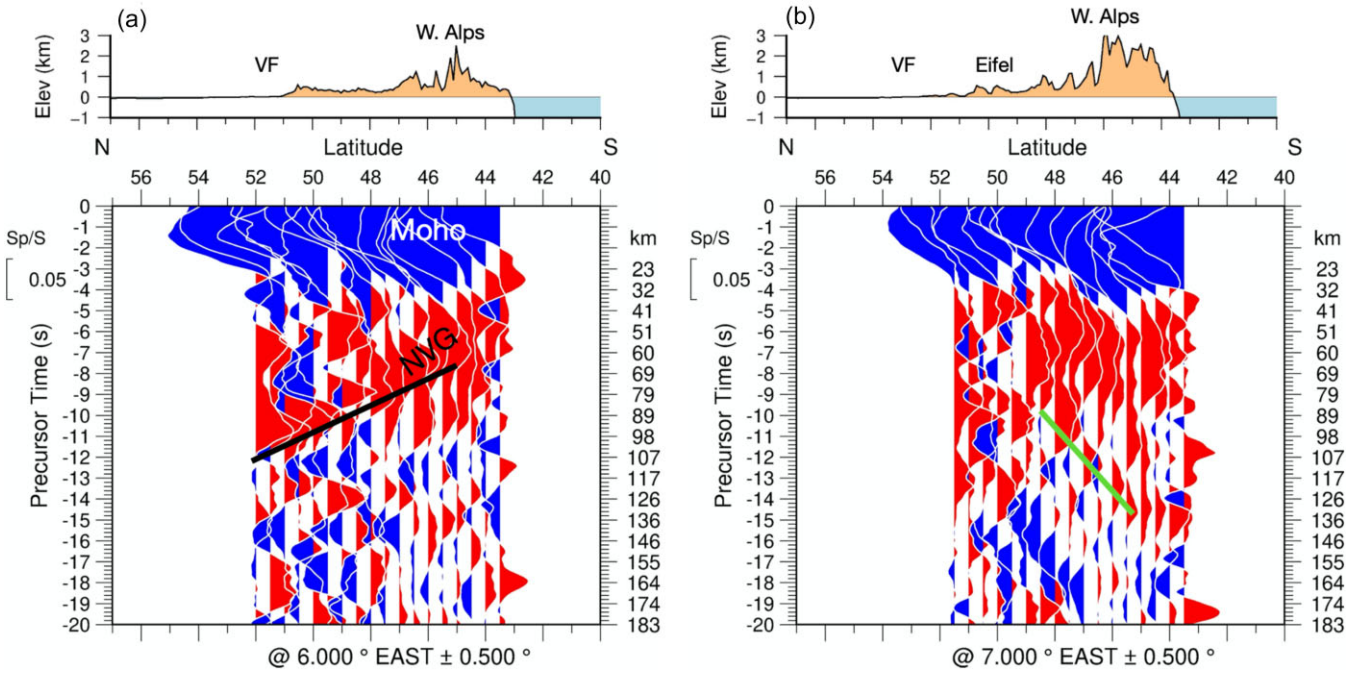

Figure 8. Two north–south profiles across the study area with a small width of 1° latitude in E–W direction, which is indicated at the bottom of the figures. The centres of the profiles in Figs 8(a) and (b) are 6 and 7°E, respectively. The elevation profiles at the top of the figures are taken along these longitudes. VF is the Variscan Front. Moho signals are marked in blue and negative velocity gradient (NVG) signals are marked in red. The piercing point depth is 100 km. The widths of the profiles in east–west direction are shown at the bottom of the figures. The spacing between stations in north–south direction is 0.5° latitude. Seismic phases below the Moho, which we used for the interpretation are marked by continuous lines. In panel (a) we see a north dipping NVG structure while in panel (b) a south dipping NVG structure is marked by a green line.

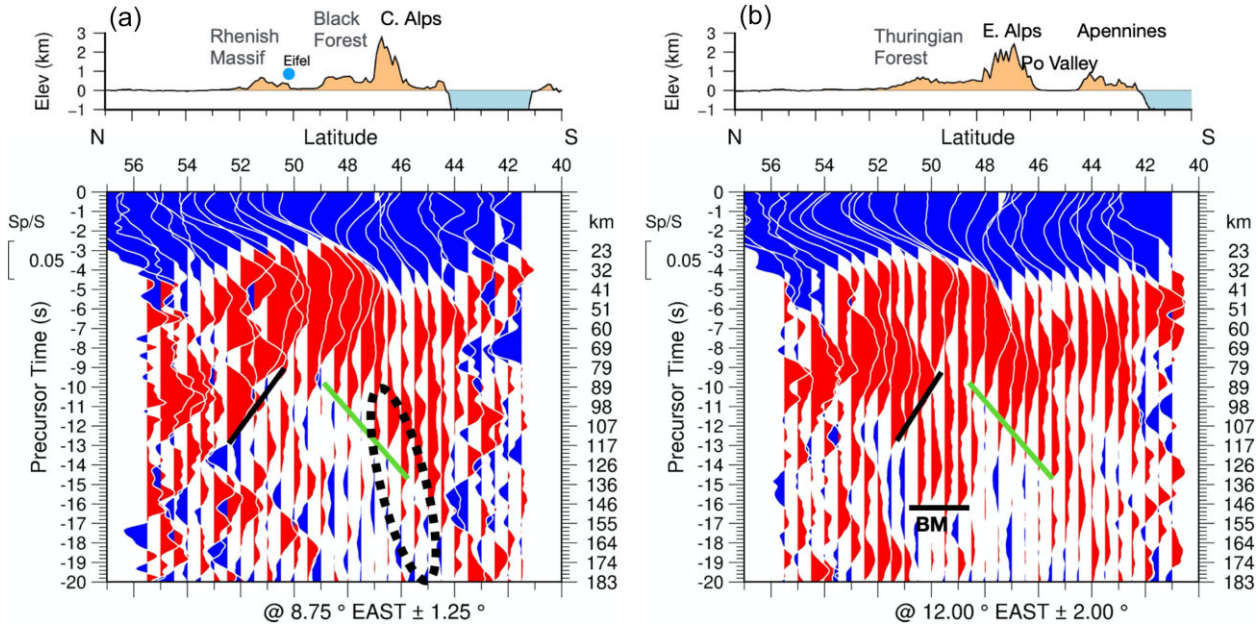

Figure 9. Two other north–south profiles similar to Fig. 8. The green line in Fig. 8(b) was transferred to (a) and (b) for easier comparison of the three profiles. This shows that the same south dipping NVG structure exists between 6.5°E (Fig. 8b) and 14°E (b). The dotted ellipse in Fig. 7(a) marks the approximative location of the south dipping lithosphere identified by Lippitsch *et al.* (2003). The black lines in Figs 7(a) and (b) mark a north dipping NVG in northern Germany. BM is the NVG below the Bohemian Massif.

very different. In Fig. 8(a) the NVG phase is clearly north dipping (black line). This structure is marked in Fig. 7 by the westernmost black arrow pointing to the north. In Fig. 8(b) a NVG phase is equally clearly south dipping (green line). The green line has been copied into the profiles of Figs 9(a) and (b) for comparison. In three profiles (Figs 8b and 9a, b), which cover the longitude region between 6.5°E and 14°E, the green lines mark the same south dipping structure. This indicates our data show a relatively homogeneous south dipping

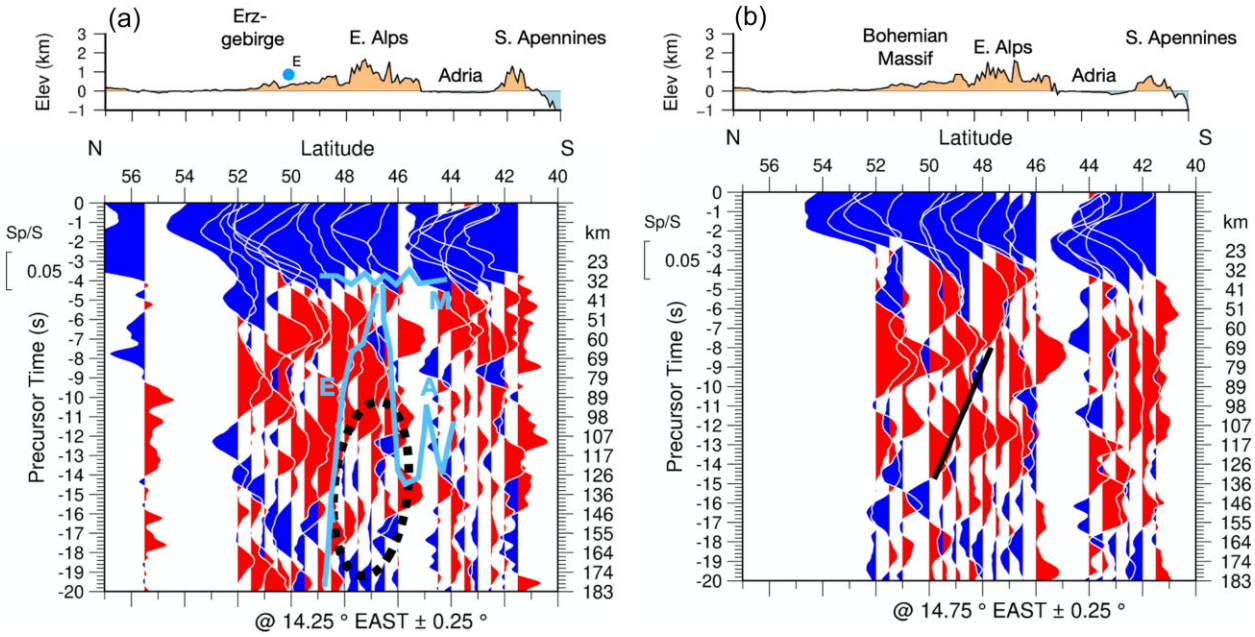

Figure 10. Two north–south profiles are shown running across the eastern Alps between 14° and 15°E longitude. The black line in Fig. 10(b) indicates a possible north dipping NVG structure. The dotted ellipse in Fig. 10(a) indicates location of the NE-dipping slab in the eastern Alps observed by Lippitsch *et al.* (2003). The cyan lines in Fig. 10(a) mark the tomographic bottom of the European lithosphere (E), of the Adriatic lithosphere (A) and of the European Moho (M) from fig. 4(c) by Handy *et al.* (2021).

NVG below large parts of the northern Alpine foreland and the main part of the Alps. Note that due to the vertical exaggeration of around a factor 8.5 the angle of dip is strongly exaggerated. The area characterized by a southerly dip stretches from about 49°N (90 km depth) to 46°N (130 km depth). Note that these are averaged values. It is marked in Fig. 7 by a green south pointing arrow. This structure could be interpreted as lower boundary of the subducting European Plate. The locations of the north dipping black NVGs in Fig. 9 are also marked in Fig. 7 by a north pointing black arrow. A very narrow profile between 14°E and 14.5°E is shown in Fig. 10(a). Apparently no clear correlation over a larger distance, which could be identified as NVG, is detectable. This is similar to the situation in Fig. 10(b). However, we marked a possible north dipping structure there with a black line. The reason is that in Fig. 11 the same north dipping NVG exists and was also marked by black line. The according arrow is also shown in Fig. 7 (see easternmost north pointing black arrow). We only marked signals as seismic discontinuities which are observed in neighbouring not overlapping profiles [green phases in Figs 8(b), 9(a) and (b); black phases in Figs 9(a), (b) and black phases in Figs 10b and 11]. More north–south profiles with one degree E–W extension and marked phase correlations are shown in the Slides 50 to 58 in the Supporting Information. There figures indicate that the north dipping NVG below northern Germany may extent further to the north than marked in Fig. 7.

The dotted ellipses in Figs 9(a) and 10(a) indicate the locations of the SE- and NE-dipping slabs in the central and eastern Alps observed by Lippitsch *et al.* (2003), respectively, using tomography. The cyan lines in Fig. 10(a) mark structures obtained by Handy *et al.* (2021) in a tomographic study (their fig. 4c). They observed the European Moho (marked M) and the European and Adriatic LABs (marked E and A, respectively). In Fig. 10(a) (across the eastern Alps between 14°E and 14.5°E) our data look extremely complicated. Also the data of Handy *et al.* (2021) and Lippitsch *et al.* (2003) show anomalies in that region.

Observations along east–west profiles

Four east–west oriented profiles with a width of 2° in latitude are shown in Figs 12(a), (b) and 13(a), (b) (see Fig. 7 for the locations). The profile shown in Fig. 12(b) is located between 46°N and 48°N and runs obliquely across the WSW–ENE striking part of the Alpine chain. The green line in Fig. 12(b) between about 7°E and 14°E highlights the eastward dipping of the NVG below most of the Alps (showing the east–west component of the dip). This interval of longitudes closely corresponds to the width of the European NVGs we see south dipping in Figs 9(a) and (b) where they are marked also in green (showing the north–south component of the dip). This indicates that the dip of the European NVG has a south dipping as well as an east dipping component, the true dip probably being towards SSE or SE. Between about 14°E and 17°E we see in Fig. 12(b) the NVG rising eastward towards the Pannonian Basin (black line). This feature can also be seen in Figs 13(a) and (b) to the north of the Alpine Front. It is probably of Miocene age, that is related to a late asthenospheric rise in the area of the Pannonian Basin that is only partly installed within the European lithosphere.

Mantle transition zone below the central European Cenozoic Igneus Province

The mantle transition zone discontinuities at 410 and 660 km depth are attributed to phase transitions that lead to density and viscosity increases. The topography of these discontinuities is temperature dependent and is used to identify mantle flow, that is the location of slabs or plumes (Bina & Helffrich 1994; Helffrich & Wood 2001). The mantle transition zone, especially the 410 km discontinuity and a low velocity zone (LVZ) about 50 km above the 410 km discontinuity have been studied by, for example Vinnik & Farra (2007), Tauzin *et al.* (2010), Kind *et al.* (2020) and Goes *et al.* (2022). Dèzes *et al.* (2004) or Meier *et al.* (2016), for example, reviewed

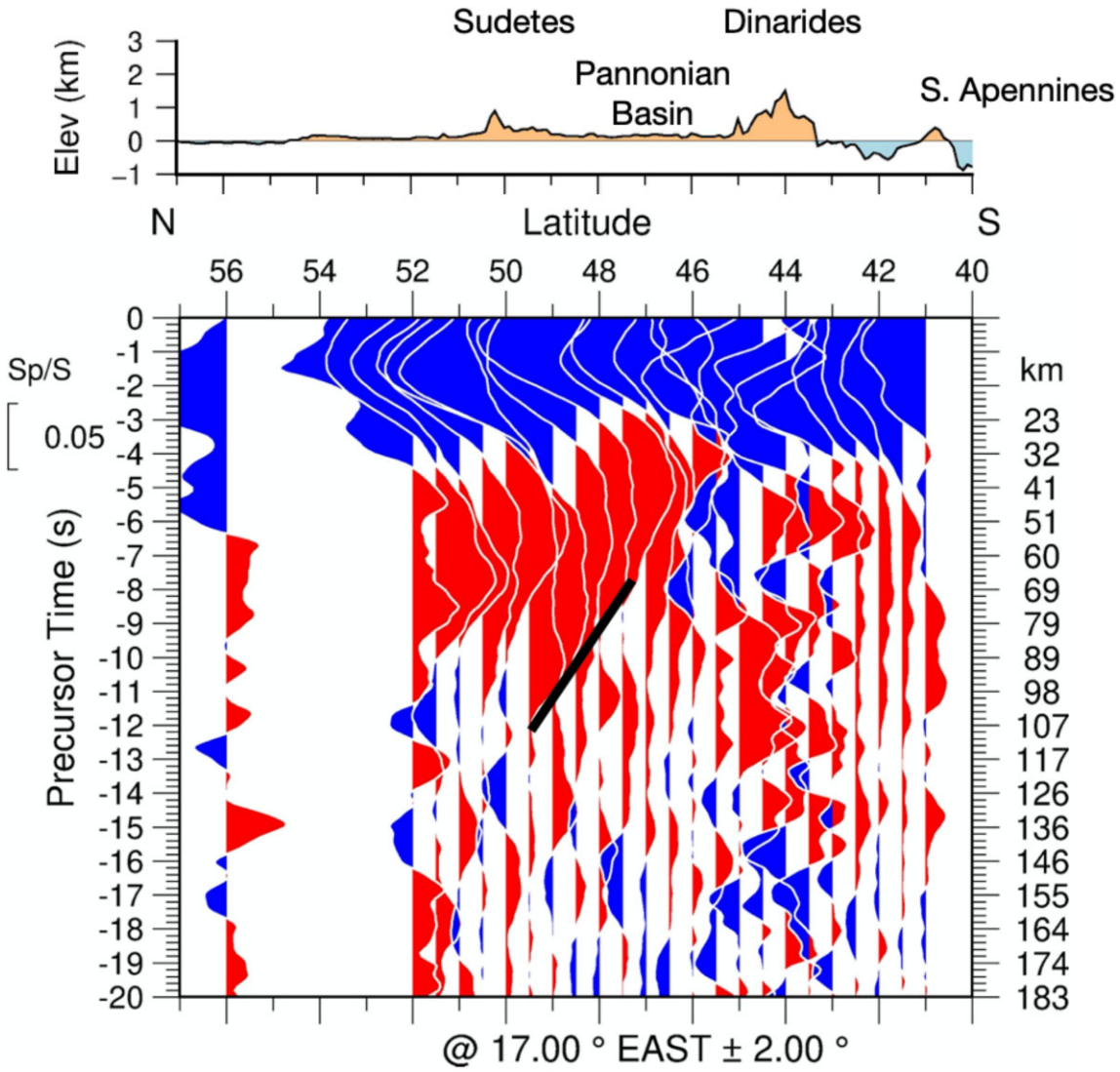

Figure 11. North–south profile located east of the Alps between 15°E and 19°E. The black line is identical with the one shown in Fig. 10(b). They indicate a broad structure of north dipping NVGs reaching from the Pannonian Basin underneath the eastern part of the Bohemian Massif and the Sudetes.

the evolution of the lithosphere in the area of the European Cenozoic Rift System and its volcanoes. The Eifel volcanic region, for example, was studied by Ritter *et al.* (2001) who found a low velocity plume-like structure extending to about 400 km depth using seismic tomography. Budweg *et al.* (2006) found, using receiver functions, a depression of the 410 by 15–25 km below the Eifel plume and explained it by a temperature increase of 200–300 °C. Seiberlich *et al.* (2013) found a thinner lithosphere in the Eifel region and Dahm *et al.* (2020) mapped a magma reservoir in the crust. However, there is an alternative explanation of the central European volcanoes, besides the plume hypothesis. Bourgeois *et al.* (2007), for example, interpreted these volcanoes as being caused by lithospheric deformations related to the Alpine orogeny. A discussion of these two interpretations is given by Koptev *et al.* (2021). In a tomographic study Plomerová *et al.* (2016) found no plume-like structure below the Eger Graben. Instead, they found a velocity decrease in the upper 200 km, which they interpreted as the possible source of the volcanoes.

The data presented in Fig. 14 show the structure of the uppermost mantle along an east–west profile approximately along the latitude that hosts the three volcanic areas marked by blue dots in Fig. 7 (Eifel, Vogelsberg and approximately the Eger Graben volcanoes). The profile in Fig. 14 is 1° wide in latitude and centred at 49.5°N. The piercing points were chosen at 300 km depth in order to focus on the discontinuities around 410 km depth and several tens of kilometres above it. Fig. 14 clearly shows a phase of blue waveforms, which is the well-known global seismic discontinuity at 410 km depth (marked 410 and by a black line). Above the 410 km discontinuity we see a second discontinuity of red signals, which indicates velocity reduction (marked LVZ and by a green line). This discontinuity is less well known and is probably caused by an increase in the amount of water (Bercovici & Karato 2003; Liu *et al.* 2018). It appears to exist globally, but not as a laterally continuous signal (Vinnik & Farra 2007; Geissler *et al.* 2008; Tauzin *et al.* 2010; Kind *et al.* 2013). Both discontinuities (410 and LVZ) are found at their usual depth below the Eifel and Vogelsberg volcanoes. This means that there is probably no indication of a temperature increase directly beneath these volcanoes near 400 km depth. In the contrary, looking at the 410 and LVZ signals beneath the Eger Graben volcanoes reveals that both these discontinuities are rising there.

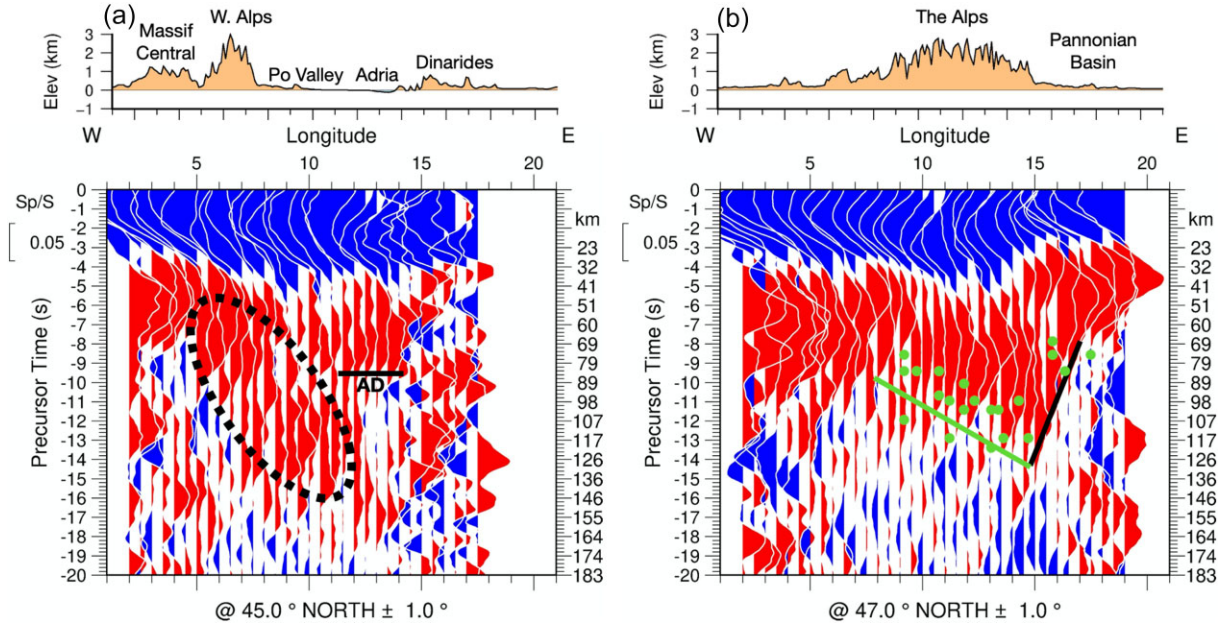

Figure 12. Two east–west profiles. (a) Profile between 44°N and 46°N from the western Alps along the Po Valley to the Dinarides. The dotted ellipse marks low velocity anomalies running from the western Alps across the Po Valley all the way to the Adriatic Sea. The black line near 80 km depth probably marks the Adriatic NVG. (b) Profile between 46°N and 48°N. The green line shows the same structure (but east dipping) like the south dipping green lines in Figs 8(b) and 9(a), (b). The green dots mark the location of the LAB observed by Bianchi *et al.* (2014) using receiver functions.

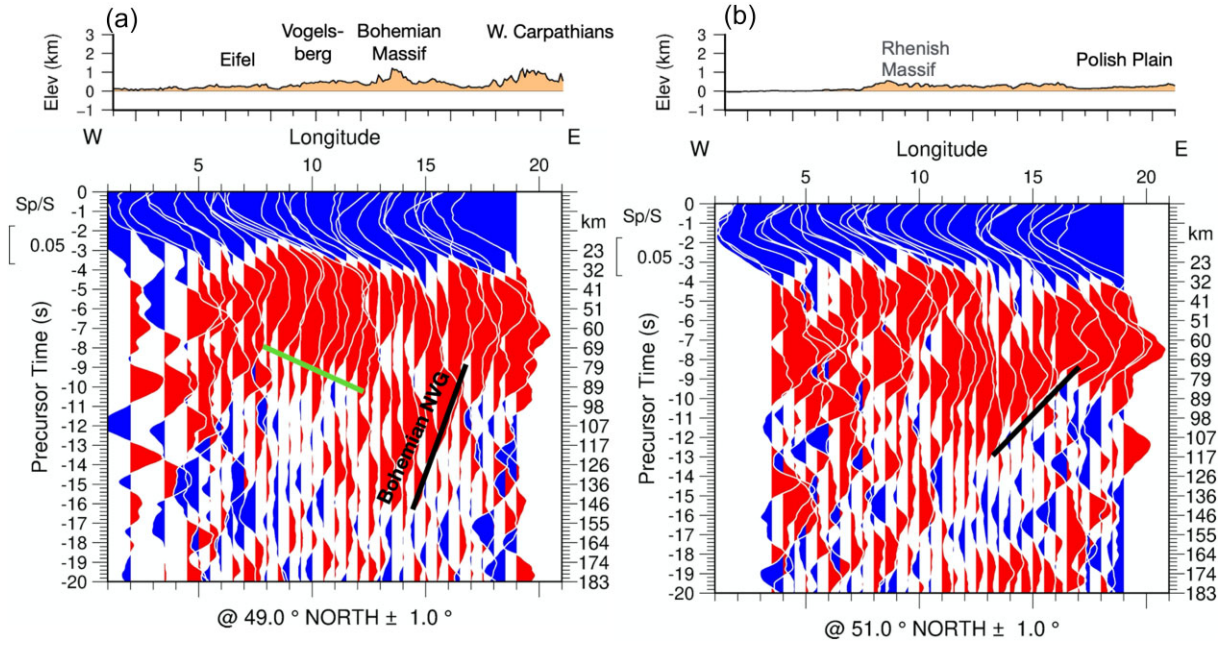

Figure 13. Two east–west profiles located north of the Alps. The green line in (a) marks the northerly continuation of the eastward dipping lithosphere below the Alps. The black lines mark the eastward shallowing lithosphere below the Bohemian Massif.

Lombardi *et al.* (2009) did not observe shallowing of the 410 below the Bohemian Massif in a *P*-receiver function study. They did not observe low velocity zone above the 410.

However, we note that the updoming of the green and the black signals below the Eger Graben is not parallel. This indicates that upper mantle velocity changes above both discontinuities can not be the cause of the updoming of both discontinuities. However, to our knowledge, it is not yet sufficiently clear what causes the updoming of the LVZ.

INTERPRETATION AND DISCUSSION

Moho

Our Moho results essentially confirm those of Grad *et al.* (2009), which are obtained with different methods, especially within the Variscan Europe (see Fig. 6b). Larger disagreements are observed in some of the Alpine regions (eastern Alps and at the southern Alpine Front), in Scandinavia and in northern Germany north of the Variscan Front. In these regions the differences between our

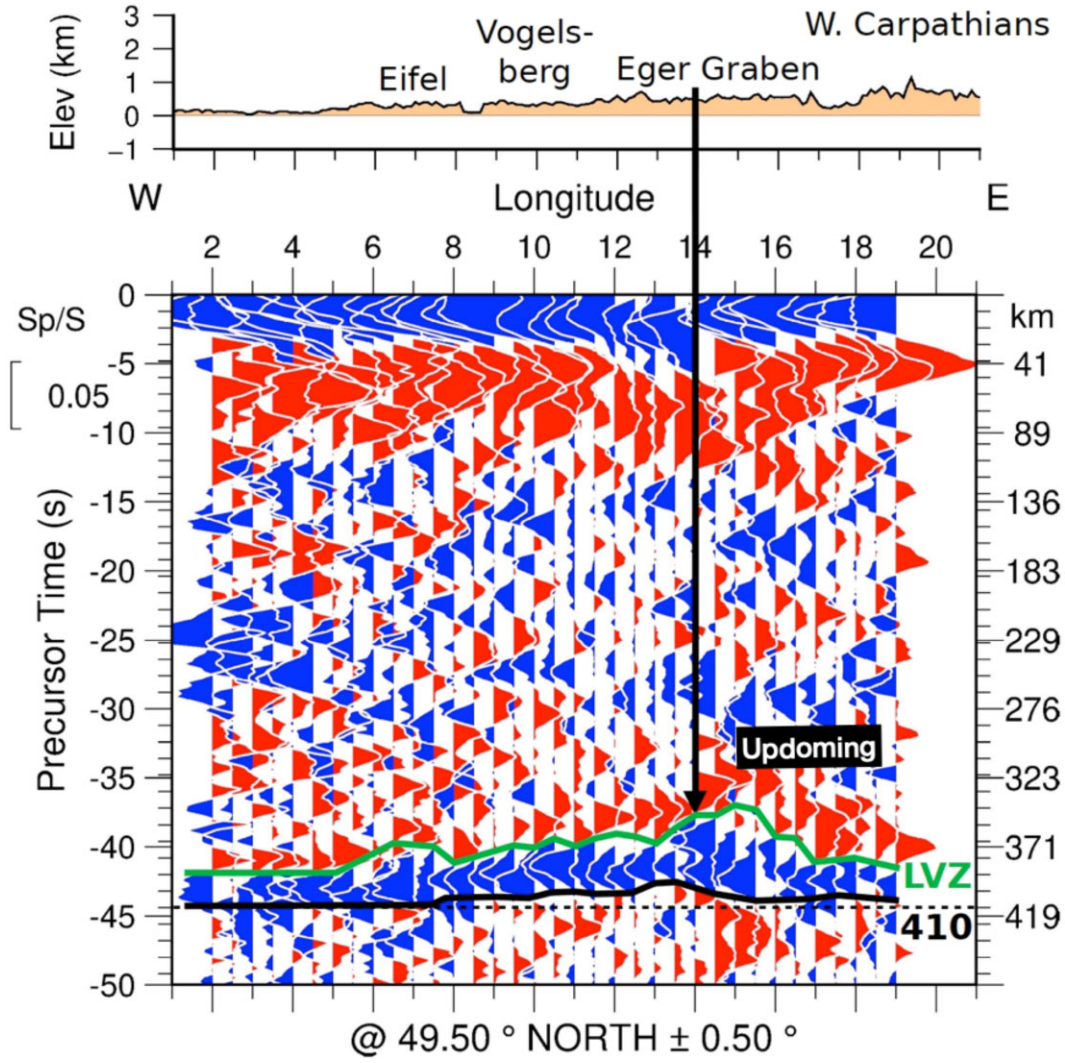

Figure 14. East–west profile along 50°N to about 450 km depth. The location of the Eifel, Vogelsberg and Eger Graben volcanoes is marked in the topographic profile at the top the figure. The 410 km discontinuity is marked along with a negative discontinuity (LVZ) above the 410 km discontinuity.

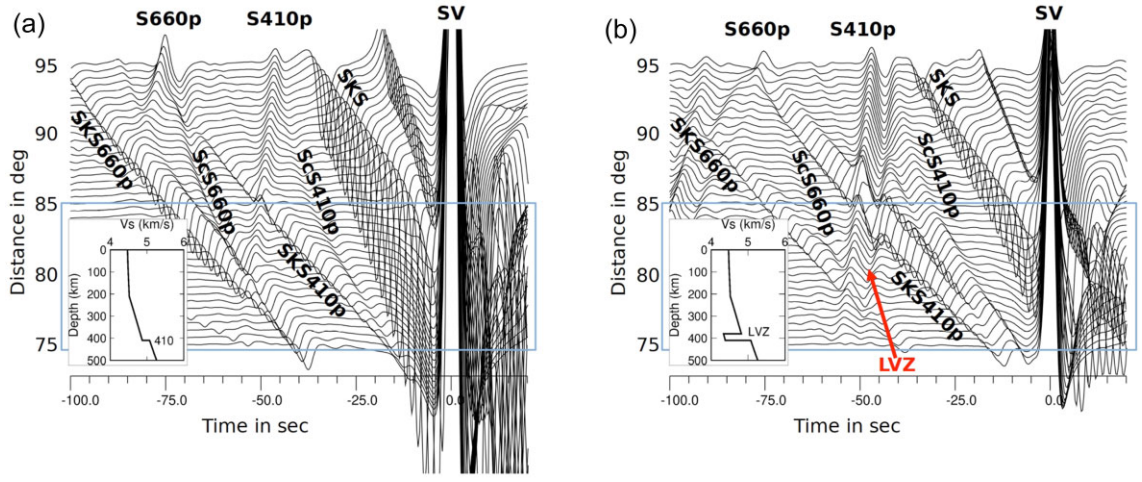

Figure 15. (a) Theoretical seismograms computed with the reflectivity method of the converted phases from the 410 (S410p) and 660 km (S660p) discontinuities for the IASP91 global model. (b) Similar theoretical seismograms for the same model but with a 30 km zone above the 410 km discontinuity with velocity reductions of 10 per cent.

data and those of Grad *et al*. are at many sites larger than 5 km. The Alpine region is a tectonic active region where larger heterogeneities are expected. The reason for larger heterogeneities of the Moho in Scandinavia is not clear.

In the Supporting Informations (Slides 5–29) we show each of the Moho signals used together with its SV signals that generate the Moho conversions. The SV signals are shifted and overlaid with the Moho signals until the optimal similarity is reached. This permits easy verification of the measured Moho precursor times.

E–W profile along the Po Valley

The collision and deformation processes of the Adriatic and European plates have been discussed in many papers; we refer, for example, to Schmid *et al.* (2004) and Handy *et al.* (2021). Particularly interesting are the slab structures, which so far were mainly studied with tomographic methods. Kästle *et al.* (2018, 2020) have compared results of different tomographic studies, which we here compare with our results of studies of S-to-P converted teleseismic waves. In their fig. 3 Kästle *et al.* (2020) show several body and surface wave tomographic profiles from different authors crossing the Alpine region. Their approximately west–east oriented profile A is shown in their fig. 3 (first published in Kästle *et al.* 2018) runs from the western Alps across the Po Plain just south of latitude 45°N, touching the northern rim of the Apennines. Hence it overlaps with the location of our E–W profile shown in Fig. 12(a). In this figure we marked with a dotted ellipse a NVG zone that, according to Kästle *et al.* (2020) consists of two slabs, European and Adriatic (their fig. 3a). We also marked a NVG zone below the easternmost Po Plain (at about 80 km depth) and the northernmost Adriatic Sea by a black line (Fig. 12a). The same profile is also shown in Slides 63a and 64a in the Supporting Information with narrower profiles to make the correlation even more clear. Inside the ellipse (Fig. 12a) we see many NVG signals; there is no single phase, which could be interpreted as representing a LAB. This diffuse pattern is probably due to the fact that this ellipse encloses mantle domains belonging to both European and Adriatic lithosphere according to the interpretations of the tomography provided by both Kästle *et al.* (2018) and Handy *et al.* (2021). The entire region appears very heterogeneous and produces many scattered NVG signals that are, in general, easterly dipping all the way from the western Alps below the Po Valley and the northern most Apennines to the easternmost Po Plain. In any case, the dotted ellipse in Fig. 12(a), highlighting the results of Kästle *et al.* (2018), agrees well with our NVG signals enclosed in this ellipse. The tomographic results of other authors shown in fig. 3 by Kästle *et al.* (2020) are taken from Lippitsch *et al.* (2003), Koulakov *et al.* (2009) and Zhao *et al.* (2016). They exhibit significantly steeper high velocity patterns, located further in the west and that do not reach easternmost Po plain. There is another tomographic study using surface waves and showing a depth profile between the western Alps and the Dinarides (El-Sharkawy *et al.* 2020; Fig. 8, Profile B). They observed a high velocity anomaly between the western Alps and the Adria between 100 and 200 km depth, which agrees with our results and those by Kästle *et al.* (2020). Still another body wave tomography study was performed by Paffrath *et al.* (2021b). They observed a low velocity anomaly between western Alps and Adria in the depth range between about 100 and 200 km (their fig. 14a profile P1), where Kästle *et al.* (2020) observed high velocity anomalies and we observed negative velocity gradients. Converted waves are sensitive to velocity ratios at discontinuities, not to absolute velocities. Tomographic studies are sensitive to velocities. It seems possible, however, that positive or negative velocity discontinuities may exist within greater areas characterized by high or low velocity anomalies. Hence, it seems possible that converted waves observe velocity reductions within tomographic high or low velocity anomalies.

N–S profiles across the Alps and their foreland

Figs 9(a) and 10(a) allow for a comparison with the mantle tomography of Lippitsch *et al.* (2003). In Fig. 9(a) we marked the approximate location of the south dipping positive velocity anomaly assigned to the European Plate (Lippitsch *et al.* 2003, their fig. 12, profile B) that runs NW–SE and intersects with our profile at about 10°E. The agreement seems to be very good. In Fig. 10(a) the dotted ellipse encloses the northeast dipping anomaly of Lippitsch *et al.* (2003, their fig. 12, profile C) attributed to the Adriatic Plate by these authors. It intersects our profile at about 14°E and is located at around 46°N. There is no signal within the location of the ellipse in our Fig. 10(a). Fig. 10(b) shows an indication of a northerly dipping NVG, which continues further towards the east as can be seen in Fig. 11. The structure of the mantle lithosphere below the eastern Alps has also been studied by Bianchi *et al.* (2014) using *P*- and *S*-receiver functions. We plotted LAB depths from their EW profiles (their Fig. 9, profiles D and E) into our EW profile shown in Fig. 12(b) (green dots). The agreement with our data is very good. The east dipping structures within the mantle lithosphere below the Alpine chain are thus confirmed by surface wave and other receiver function data. If we compare the Figs 12(b) and 13(a), we see an astonishing similarity (not identity) of the east–west components of the NVG structure below the Alps and their far northern foreland. Also below the Po Valley, the main visible feature is an east dipping NVG (Fig. 12a). That means that there are between the Po Valley in the south and about 50°N, where the line of the volcanoes is located, significant similarities in the NVG structures.

The LAB in northern Germany

There are *S* receiver function studies of the LAB structure in northern Central Europe that confirm our observations of a shallow NVG at 49–50°N and a deeper LAB further north. Knapmeyer-Endrun *et al.* (2017) observe in the region from about 8°E to 24°E and 48 to 52°N the LAB near 10 s precursor time, which corresponds to about 90 km depth (see their Fig. 4). Also Geissler *et al.* (2010) using *S*-receiver functions in northern Germany observed LAB depths near 100 km near 50°N and about 120 km further north. In an area around the northeastern part of the Bohemian Massif Geissler *et al.* (2012) observed, also in an *S*-receiver function study, LAB depths between 80 and 110 km. They used higher resolution piercing point cells of 0.5° × 0.5° latitude and longitude and observed relatively large scattering of the LAB depths in this area (see Geissler *et al.* 2012; Fig. 6). Heuer *et al.* (2007) observed LAB depths near 100 km in the northern part of the Bohemian Massif and LAB depths close to 150 km in the southern part of the Bohemian Massif. At about 12.5–14.5°E and 46–49°N Plomerová *et al.* (2022) obtained with tomography high velocity anomalies which have been interpreted as a double north dipping slab. However, our Fig. 9(b) shows at the same latitudes and at 10–14°E a clearly south dipping NVG, but further north we see indications of a north dipping NVG.

Comparing different continent–continent collision zones we find on the basis of receiver function studies, performed in the Alps and in Tibet, subduction only of the mantle lithosphere, not the crust,

down to about 150 km depth. This means the crust is separated from the mantle lithosphere and stays at a shallower depth. In the Pamir collision zone exists deep seismicity and the crust is observed down to about 150 km. In the Pamir and Tibet a crustal doubling was observed, apparently not in the Alps (Schneider *et al.* 2019).

Maximum Moho depth

We also compare our observations with the results of a Moho study by Mroczek *et al.* (2023) in the eastern Alps based on receiver function analysis. In their fig. 2(b) they show a north–south *P*-receiver function profile at 13.3°E. A parallel profile of *S*-receiver functions was shown by Kind *et al.* (2021, their figs 8a, b). In both papers the deepest Moho was observed near 60 km below the Tauern Window. The Moho trough there was also observed by Hetényi *et al.* (2018). Mroczek *et al.* (2023), however, postulate a continuation of the south dipping Moho further to the east (at 14° longitude, their fig. 3b) where a depth of about 150 km depth is inferred based on the SH component of the *P*-receiver function. They also noted, that their Moho observations of the SH component of the *P* receiver functions follow in parallel the NVG data of Kind *et al.* (2021) down to about 150 km depth. The Moho depth observations of Kind *et al.* (2021) in S-to-P conversions, however, do not exceed 60 km at the same location. Moho depths observations of 150 km also disagree with other previous studies concerning the depth of the Moho in that area located east of the Tauern Window (e.g. Grad *et al.* 2009; Spada *et al.* 2013). We think finding a stable model to explain a Moho signal at 150 km depth observed in the SH component of *P*-receiver functions would require considering anisotropy and 3-D inhomogeneity.

The 410 km discontinuity

Knapmeyer-Endrun *et al.* (2017) suggest that no low velocity zone above the 410 km discontinuity is required to produce a negative signal following the 410 signal. They suggest instead that these signals could be caused by interference of the 410 signal with ScS660p and SKS660p. Yuan *et al.* (2006) discussed this question already using theoretical seismograms. Fig. 15 shows theoretical seismograms computed with a version of the reflectivity method by Kind (1985), which permits different structures at the source and receiver sides. The IASP91 model was used for the computation. However, we omitted the crust at the source and receiver sides for simplicity. Fig. 15(b) shows theoretical seismograms with a low velocity zone added to the model above the 410 km discontinuity. This zone is 30 km thick and its velocities are reduced by 10 per cent. The 410 and LVZ phases are clearly visible in spite of conversions from ScS and SKS at the 410 and 660 km discontinuities. This indicates that the observations of a low velocity zone above the 410 km discontinuity in the S-to-P converted phases is real and not an effect of superposition of several other phases.

CONCLUSIONS

Simple stacking of seismic traces is the oldest method to raise weak signals above the noise level. We have shown that this version of stacking without any modifications of the waveforms, like for example deconvolution, is able achieve this. We have also shown that conventional receiver function processing using deconvolution might produce erroneous signals if deconvolution is used before stacking. Deconvolution after plain stacking produces similar results like plain stacking. This applies essentially to weak signals like, for example conversions from below the Moho. We have also shown that in many cases plain stacking of converted waves produces high quality Moho signals, which can be directly compared with the signal forms of the converting SV signal for improved identification of Moho signals. We compared Moho depth determinations obtained with our new method with those obtained by Grad *et al.* (2009) and obtained in the Variscan Europe good agreements within 5 km. In the Alpine region and in Scandinavia we found larger disagreements, which might be due to larger heterogeneities there. The relative homogeneous Moho in the Variscan Europe may be the result of a reworking of the crust-mantle boundary after the Variscan orogenies (Meier *et al.* 2016).

The most significant results obtained with our method is the improved imaging of seismic discontinuities in the upper 200 km in the Alpine region and its northern foreland. In this region we found coherent signals of negative seismic discontinuities, which might be related to the lower boundary of the involved plates. In the entire region along the volcanic chain from the Eifel to the Eger Graben and in the south approximately from the western to the eastern Alps we found indications of the south dipping lower boundary of the European Plate. The Moho is not following the lower boundary of the plate. Below the central and eastern Alps the European Plate has also an east dipping component. Such an east dipping structure is also imaged beneath the western Alps and the Adriatic Plate beneath the Po Plain, which may have a thickness of about 80 km. Surrounding this southeast dipping part of the European lithosphere in the west, in the north and the east we observe a northern dip of the European lithosphere.

ACKNOWLEDGMENTS

This research was carried out within the AlpArray and SWATH-D projects, which have been funded by the Deutsche Forschungsgemeinschaft within the Priority Program ‘Mountain Building Processes in Four Dimensions (MB-4D)’ and within the Project KI 314/35-1 and by the GeoForschungsZentrum Potsdam.

The following networks have contributed data to this study: PASSEQ (7E), Albanian Seismological Network (AC), Belgian Seismic Network (BE), Bayernnetz (BW), Switzerland Seismological Network (CH), Croatian Seismograph Network (CR), Czech Regional Seismic Network (CZ), Danish Seismological Network (DK), Estonian Seismic Network (EE), Northern Finland Seismological Network (FN), RESIF and other broad-band and accelerometric permanent networks in metropolitan France (FR), GEOFON (GE), German Regional Seismic Network (GR), Regional Seismic Network of north western Italy (GU), Finish National Seismic Network (HE), Hungarian National Seismological Network (HU), Global Seismograph Network—IRIS/USGS (IU), Italian National Seismic Network (IV), Mediterranean Very Broad-band Seismographic Network (MN), Netherlands Seismic and Acoustic Network (NL), Austrian Seismic Network (OE), North-East Italy Seismic Network (OX), Polish Seismological Network (PL), CEA/DASE Seismic Network (RD), Romanian Seismic Network (RO), Province Südtirol (SI), Serbian Seismological Network (SJ), Slovak National Seismic Network (SK), Seismic Network of the Republic of Slovenia (SL), Trentino Seismic Network (ST), SXNET Saxon Seismic

Network (SX), Thüringer Seismologisches Netz (TH), Eifel Plume (XE), EASI Eastern Alpine Seismic Investigations (XT), AlpArray (Z3), TOR-TE (ZA), SVEKALAPKO (ZB), TOR-TO (ZC), Transalp II (ZO), SWATH-D (ZS), Bohema (ZV) and JULS (ZW).

Members of the AlpArray Working Group can be found at: http://www.alparray.ethz.ch/en/seismic_ network/backbone/data-policy-and-citation/and members of the SWATH-D Working Group at: https://doi.org/10.14470/mf7562601148.

SUPPLEMENTARY DATA

Supplementary data are available at *GJI* online.

DATA AVAILABILITY

The data used are publicly available from the EIDA portals (e.g. http://www.orfeus-eu.org/data/eida, ORFEUS 2021).

REFERENCES

Abt, D.L., Fischer, K.M., French, S.W., Ford, H.A., Yuan, H. & Romanowicz, B., 2010, North American lithospheric discontinuity structure imaged by Ps and Sp receiver functions, *J. geophys. Res.,* **115**(B9), doi:10.1029/2009JB006914.

Baer, M. & Kradolfer, U., 1987. An automatic phase picker for local and teleseismic events, *Bull. seism. Soc. Am.,* **77**(4), 1437–1445.

Bercovici, D. & Karato, S.-I., 2003. Whole-mantle convection and the transition-zone water filter, *Nature,* **425**(6953), 39–44.

Bianchi, I., Miller, M.S. & Bokelmann, G., 2014. Insights on the upper mantle beneath the eastern Alps, *Earth planet. Sci. Lett.,* **403,** 199–209.

Bianchi, I., Ruigrok, E., Obermann, A. & Kissling, E., 2021. Moho topography beneath the European Eastern Alps by global-phase seismic interferometry, *Solid Earth,* **12,** 1185–1196.

Bina, C.R. & Helffrich, G., 1994. Phase transition Clapeyron slopes and transition zone seismic discontinuity topography, *J. geophys. Res.,* **99,** 15 853–15 860.

Bourgeois, O., Ford, M., Diraison, M., Le Carlier de Veslud, C., Gerbault, M., Pik, R., Ruby, N. & Bonnet, S., 2007. Separation of rifting and lithospheric folding signatures in the NW-Alpine foreland, *Int. J. Earth Sci. (Geol. Rundsch.),* **96,** 1003–1031 .

Budweg, M., Bock, G. & Weber, M., 2006. The Eifel Plume—imaged with converted seismic waves, *Geophys. J. Int.,* **166,** 579–589.

Dahm, T. *et al.*, 2020. Seismological and geophysical signatures of the deep crustal magma systems of the Cenozoic volcanic fields beneath the Eifel, Germany, *Geochem. Geophys. Geosyst.,* **21,** e2020GC009062. .

Dèzes, P., Schmid, S.M. & Ziegler, P.A., 2004. Evolution of the European Cenozoic Rift System: interaction of the Alpine and Pyrenean orogens with their foreland lithosphere, *Tectonophysics,* **389,** 1–33.

El-Sharkawy, A., Meier, T., Lebedev, S., Behrmann, J.H., Hamada, M., Cristiano, L., Weidle, C. & Köhn, D., 2020. The slab puzzle in the Alpine-Mediterranean Region: insights from a new, high-resolution, shear wave velocity model of the upper mantle, *Geochem. Geophys. Geosyst.,* **21,** e2020GC008993, doi:10.1029/2020GC008993.

Geissler, W.H., Kämpf, H., Skácelová, Z., Plomerová, J., Babuška, V. & Kind, R., 2012. Lithosphere structure of the NE Bohemian Massif (Sudetes)—a teleseismic receiver function study, *Tectonophysics,* **564–565,** 12–37.

Geissler, W.H., Kind, R. & Yuan, X., 2008. Upper mantle and lithospheric heterogeneities in Central and Eastern Europe seen by teleseismic receiver functions, *Geophys. J. Int.,* **174,** 1–26.

Geissler, W.H., Sodoudi, F. & Kind, R., 2010. Thickness of the central and eastern European lithosphere as seen by S-receiver functions, *Geophys. J. Int.,* **181,** 604–634.

Goes, S., Yu, C., Ballmer, M.D., Yan, J. & van der Hilst, R.D., 2022. Compositional heterogeneity in the mantle transition zone, *Nat. Rev. Earth Environ.,* **3,** 533–550.

Grad, M. & Tiira, T., 2012. Moho depth of the European Plate from teleseismic receiver functions, *J. Seismol.,* **16,** 95–105.

Grad, M. & Tiira, T., ESC Working Group, 2009. The Moho depth map of the European Plate, *Geophys. J. Int.,* **176,** 279–292.

Handy, M.R., Schmid, S.M., Marcel Paffrath, M. & Friederich, W., the AlpArray Working Group, 2021. Orogenic lithosphere and slabs in the greater Alpine area—interpretations based on teleseismic P-wave tomography, *Solid Earth,* **12,** 2633–2669.

Heit, B., Weber, M., Tilmann, F., Haberland, C., Jia, Y., Carraro, C. & Pesaresi, D., 2017. The SWATH-D seismic network in Italy and Austria, GFZ Data Services, doi:10.1016/2002gl014911.

Helffrich, G.R. & Wood, B.J., 2001. The Earths mantle. *Nature,* **412,** 501–507.

Hetényi, G. *et al.*, 2018. The AlpArray Seismic Network: a large-scale European experiment to image the Alpine orogeny, *Surv. Geophys.,* **39,** 1009–1033.

Heuer, B., Kämpf, H., Kind, R. & Geissler, H., 2007. Seismic evidence for whole lithosphere separation between Saxothuringian and Moldanubian tectonic units in central Europe, *Geophys. Res. Lett.,* **34**(9), doi:10.1029/2006GL029188.

Hua, J., Fischer, K.M., Becker, T.W., Gazel, E. & Hirth, G., 2023. Asthenospheric low-velocity zone consistent with globally prevalent partial melting, *Nat. Geosci.,* **16,** 175–181.

Kästle, E.D., El-Sharkawy, A., Boschi, L., Meier, T., Rosenberg, C., Bellahsen, N., Cristiano, L. & Weidle, C., 2018. Surface wave tomography of the Alps using ambient-noise and earthquake phase velocity measurements, *J. geophys. Res.,* **123**(2), 1770–1792.

Kästle, E.D., Rosenberg, C., Boschi, L., Bellahsen, N., Meier, T. & El-Sharkawi, A., 2020. Slab break-offs in the Alpine subduction zone, *Int. J. Earth Sci.,* **109,** 587–603.

Kennett, B.L.N. & Engdahl, E.R., 1991. Travel times for global earthquake location and phase identification, *Geophys. J. Int.,* **105,** 429–465.

Kind, R. *et al.*, 2002. Seismic images of crust and upper mantle beneath Tibet: evidence for Eurasian plate subduction, *Science,* **298,** 1219–1221.

Kind, R. *et al.* 2013. Scandinavia: a former Tibet?, *Geochem. Geophys. Geosyst.,* **14,** 4479–4487.

Kind, R., 1974. Long range propagation of seismic energy in the lower lithosphere, *J. Geophys,* **40,** 189–202.

Kind, R., 1985. The reflectivity method for different source and receiver structures and comparison with GRF data, *J. Geophys.,* **58,** 146–152.

Kind, R., Handy, M.R., Yuan, X., Meier, T., Kämpf, H. & Somroo, R., 2017. Detection of a new sub-lithospheric discontinuity in central Europe with S-receiver functions, *Tectonophysics,* **700–701,** 19–31.

Kind, R., Mooney, W. & Yuan, X., 2020. New insights into structural elements of the upper mantle beneath the contiguous United States from S-to-P converted seismic phases, *Geophys. J. Int.,* **222,** 646–659.

Kind, R., Stefan, S.M., Yuan, X., Heit, B. & Meier, T., the Alparray & SWATH-D Working Groups, 2021. Moho and uppermost mantle structure in the Alpine area from S-to-P converted waves, *Solid Earth,* **12,** 2503–2521.

Kind, R., Yuan, X. & Kumar, P., 2012. Seismic receiver functions and the lithosphere-asthenosphere boundary, *Tectonophysics,* **536-537,** 25–43.

Knapmeyer-Endrun, B., Krüger, F. & Geissler, W.H., 2017. Upper mantle structure across the Trans-European Suture Zone imaged by S-receiver functions, *Earth planet. Sci. Lett.,* **458,** 429–441.

Knapmeyer-Endrun, B. & Krüger, F., PASSEQ Working Group, 2014. Moho depths across the Trans-European Suture Zone fro P- and S-receiver functions, *Geophys. J. Int.,* **197,** 1048–1075.

Koptev, A., Cloetingh, S. & Ehlers, T.A., 2021. Longevity of small-scale ('baby') plumes and their role in lithospheric break-up, *Geophys. J. Int.,* **227,** 439–471.

Kosarev, G., Kind, R., Sobolev, S.V., Yuan, X., Hanka, W. & Oreshin, S., 1999. Seismic evidence for a detached Indian lithospheric mantle beneath Tibet, *Science,* **283,** 1306–1309.

Koulakov, I., Kaban, M., Tesauro, M. & Cloetingh, S., 2009. P-and S-velocity anomalies in the upper mantle beneath Europe from tomographic inversion of ISC data, *Geophys. J. Int.,* **179**(1), 345–366.

Krueger, H.E., Gama, I. & Fischer, K.M., 2021. Global patterns in cratonic mid-lithospheric discontinuities from sp-receiver functions, *Geochem. Geophys. Geosyst.,* **22**(6), e2021GC009819, doi:10.1029/2021GC009819.

Kumar, P., Kind, R. & Yuan, X., 2010. Receiver function summation without deconvolution, *Geophys. J. Int.,* **180**(3), 1223–1230.

Li, X., Kind, R., Priestley, K., Sobolev, S.V., Tilmann, F., Yuan, X. & Weber, M., 2000. Mapping the Hawaiian plume with converted seismic waves, *Nature,* **405,** 938–941.

Lippitsch, R., Kissling, E. & Ansorge, J., 2003. Upper mantle structure beneath the Alpine orogen from high-resolution tele-seismic tomography, *J. geophys. Res.,* **108**(B8), doi:10.1029/2002JB002016.

Liu, Z., Park, J. & Karato, S., 2018. Seismic evidence for water transport out of the mantle transition zone beneath the European Alps. *Earth Planet. Sci. Lett.,* **482,** 93–104

Lombardi, D., Braunmiller, J., Kissling, E. & Giardini, D., 2009. Alpine mantle transition zone imaged by receiver functions, *Earth planet. Sci. Lett.,* **278**(3-4), 163–174.

Meier, T., Soomro, .A., Viereck, L., Lebedev, S., Behrmann, J.H., Weidle, C., Cristiano, L. & Hanemann, R., 2016. Mesozoic and cenozoic evolution of the Central European lithosphere, *Tectonophysics,* **692,** 58–73.

Meissner, R., DEKORP Research Group, 1991. The DEKORP surveys: major results in tectonic and reflective styles, in *Continental Lithosphere: Deep Seismic Reflections,* AGU Geodynamics Series, Vol. **22,** pp. 69–76, eds Meissner, R., Brown, L., Duerbaum, H.-J., Franke, W., Fuchs, K. & Seifert, E., AGU.

Mroczek, S., Tilmann, F., Pleuger, J., Yuan, X. & Heit, B., 2023. Establishing the eastern alpine-dinaric transition with teleseismic receiver functions: evidence for subducted European crust, *Earth planet. Sci. Lett.,* **609,** doi:10.1016/j.epsl.2023.118096.

Paffrath, M. & Friederich, W., Alparray and SWATH-D Working Groups, 2021a. Teleseismic P waves at the AlpArray seismic network: wave fronts, absolute travel times and travel-time residuals, *Solid Earth,* **12**(7), 1635–1660.

Paffrath, M., Friederich, W., Schmid, S.M. & Handy, M.R., the AlpArray and AlpArray-Swath D Working Group. 2021b. Imaging structure and geometry of slabs in the greater Alpine area—a p-wave travel-time tomography using Alp Array Seismic Network data, *Solid Earth,* **12,** 2671–2702.

Plomerová, J., Munzarova, H., Vecsey, L., Kissling, E., Achauer, U. & Babuska, V., 2016. Cenozoic volcanism in the Bohemian Massif in the context of P- and S-velocity high-resolution teleseismic tomography of the upper mantle, *Geochem., Geophys., Geosyst.,* **17,** 3326–3349.

Plomerová, J., Žlebčíková, H., Hetényi, G., Vecsey, L. & Babuška, V. 2022. Two subduction-related heterogeneities beneath the eastern Alps and the Bohemian Massif imaged by high-resolution P-wave tomography, *Solid Earth,* **13,** 251–270.

Rajh, G., Stipčević, J., Živčić, M., Marijan Herak, M. & Gosar, A., the AlpArray Working Group, 2022. One-dimensional velocity structure modeling of the Earth's crust in the northwestern Dinarides, *Solid Earth,* **13,** 177–203.

Ritter, J.R.R., Jordan, M., Christensen, U.R. & Achauer, U., 2001. A mantle plume below the Eifel volcanic fields, Germany, *Earth planet. Sci. Lett.,* **186,** 7–14.

Schiffer, C., Stephenson, R.A., Petersen, K.D., Nielsen, S.B., Jacobsen, B.H., Balling, N. & Macdonald, D.I.M., 2015. A sub-crustal piercing point for North Atlantic reconstructions and tectonic implications, *Geology,* **43,** 1087–1090.

Schmid, S.M., Fügenschuh, B., Kissling, E. & Schuster, R., 2004. Tectonic map and overall architecture of the Alpine orogen, *Eclogae Geol. Helv.,* **97**(1), 3–117.

Schmid, S.M., Kissling, E., Diehl, T., van Hinsbergen, D.J. & Molli, G., 2017. Ivrea mantle wedge, arc of the Western Alps, and kinematic evolution of the Alps–Apennines orogenic system, *Swiss J. Geosci.,* **110**(2), 581–612.

Schneider, F.M. *et al.*, 2019. The crust in the Pamir: insights from receiver functions, *J. geophys. Res.,* **124,** 9313–9331.

Seiberlich, C.K.A., Ritter, J.R.R. & Wawerzinek, B., 2013. Topography of the lithosphere–asthenosphere boundary below the Upper Rhine Graben Rift and the volcanic Eifel region, Central Europe, *Tectonophysics,* **603,** 222–236.

Spada, M., Bianchi, I., Kissling, E., Agostinetti, N.P. & Wiemer, S., 2013. Combining controlled-source seismology and receiver function information to derive 3-D Moho topography for Italy, *Geophys. J. Int.,* **194,** 1050–1068.

Stammler, K., 1993. Seismic handler—programmable multichannel data handler for interactive and automatic processing of seismological analyses, *Comput. Geosci.,* **19,** 135–140.

Tauzin, B., Debayle, E. & Wittlinger, G., 2010. Seismic evidence for global low-velocity layer within the Earth's upper mantle, *Nat. Geosci.,* **3,** 718–721.

Vinnik, L. & Farra, V., 2007. Low S velocity atop the 410-km discontinuity and mantle plumes, *Earth planet. Sci. Lett.,* **262,** 398–412.

Yuan, X., Kind, R., Li, X. & Wang, R., 2006. The S receiver functions: synthetics and data example, *Geophys. J. Int.,* **165**(2), 555–564.

Zhao, L. *et al.*, 2016. Continuity of the Alpine slab unraveled by high-resolution P wave tomography, *J. geophys. Res.,* **121**(12), 8720–8737.

Ziegler, P.A. & Dèzes, P., 2006. Crustal evolution of Western and Central Europe, *Geol. Soc., Lond., Memoirs,* **32,** 43–56.